

Fusing Structure from Motion and Simulation-Augmented Pose Regression from Optical Flow for Challenging Indoor Environments[★]

Felix Ott^{a,b,d,*}, Lucas Heublein^a, David Rügamer^{b,c,d}, Bernd Bischl^{b,d} and Christopher Mutschler^a

^aFraunhofer IIS, Fraunhofer Institute for Integrated Circuits IIS, Nordostpark 84, Nuremberg 90411, Germany

^bLMU Munich, Ludwigstraße 33, Munich 80539, Germany

^cTechnical University of Dortmund, August-Schmidt-Straße 1, Dortmund 44227, Germany

^dMunich Center for Machine Learning (MCML), Ludwigstraße 33, Munich 80539, Germany

ARTICLE INFO

Keywords:

visual self-localization
structure from motion
pose regression
optical flow
pose graph optimization
recurrent pose fusion
synthetic transfer learning
challenging environment

Datasets and Source Code:

https://gitlab.cc-asp.fraunhofer.de/ottf/industry_datasets

ABSTRACT

The localization of objects is essential in many applications, such as robotics, virtual and augmented reality, and warehouse logistics. Recent advancements in deep learning have enabled localization using monocular cameras. Traditionally, structure from motion (SfM) techniques predict an object's absolute position from a point cloud, while absolute pose regression (APR) methods use neural networks to understand the environment semantically. However, both approaches face challenges from environmental factors like motion blur, lighting changes, repetitive patterns, and featureless areas. This study addresses these challenges by incorporating additional information and refining absolute pose estimates with relative pose regression (RPR) methods. RPR also struggles with issues like motion blur. To overcome this, we compute the optical flow between consecutive images using the Lucas-Kanade algorithm and use a small recurrent convolutional network to predict relative poses. Combining absolute and relative poses is difficult due to differences between global and local coordinate systems. Current methods use pose graph optimization (PGO) to align these poses. In this work, we propose recurrent fusion networks to better integrate absolute and relative pose predictions, enhancing the accuracy of absolute pose estimates. We evaluate eight different recurrent units and create a simulation environment to pre-train the APR and RPR networks for improved generalization. Additionally, we record a large dataset of various scenarios in a challenging indoor environment resembling a warehouse with transportation robots. Through hyperparameter searches and experiments, we demonstrate that our recurrent fusion method outperforms PGO in effectiveness.

1. Introduction

Accurate localization of objects is essential for various path planning applications, such as robotic systems operating in vast warehouses (Radwan et al., 2018; Löffler et al., 2018). Achieving this requires highly precise pose recognition, including both the robot's position and orientation. While some localization systems rely on LiDAR, radio, or radar-based technologies (Stahlke et al., 2022) or inertial sensors (do Monte Lima et al., 2019), visual self-localization using monocular cameras has become increasingly popular due to advancements in deep learning techniques (Kendall

et al., 2015). The effectiveness of pose estimation methods heavily depends on the invariance properties of the features used, such as scale and rotation invariance (Ott et al., 2022a).

The 3D structure of a scene can be estimated from a sequence of 2D images using structure from motion (SfM) methods (Venkataraman, 2020; Resch et al., 2015; Jiang et al., 2020; Brachmann et al., 2023; Yu et al., 2023; Li et al., 2023b), which involve camera motion estimation by detecting and matching feature points between pairs of images, and 3D structure estimation by triangulating the feature points. Absolute pose regression (APR) techniques (Kendall et al., 2015; Löffler et al., 2018; Radwan et al., 2018) use neural networks to extract features from images and estimate the 6DoF global pose of an object with respect to a known coordinate system. Classical visual odometry (VO) methods (Mansur et al., 2017) estimate camera motion by analyzing consecutive images to compute the relative pose of an object. Relative pose regression (RPR) methods (Wang et al., 2017; Iyer et al., 2018; Kreuzig et al., 2019; Idan et al., 2023) have emerged, which predict the relative pose by using convolutional neural networks (CNNs) and recurrent neural networks (RNNs). RPR methods based on optical flow, which captures the motion of pixels between two frames, are particularly promising due to their robustness to environmental changes, as evidenced by recent studies (Muller and Savakis, 2017; Muller et al., 2016; Zhou et al., 2020; Ott et al., 2020).

[★]Evaluating the performance of absolute pose regression methods, i.e., SfM and PoseNet, in challenging scenarios such as repetitive patterns, motion blur, structure-less surfaces, and difficult lighting conditions. Fusing absolute and relative poses using either PGO or recurrent networks.

*Corresponding author

✉ felix.ott@iis.fraunhofer.de (F. Ott); heubleins@iis.fraunhofer.de (L. Heublein); david.ruegamer@stat.uni-muenchen.de (D. Rügamer); bernd.bischl@stat.uni-muenchen.de (B. Bischl); christopher.mutschler@iis.fraunhofer.de (C. Mutschler)

🌐 <https://www.slds.stat.uni-muenchen.de/people/ott/> (F. Ott); <https://www.slds.stat.uni-muenchen.de/people/ruegamer/> (D. Rügamer); <https://www.statistik.uni-muenchen.de/personen/professoren/bischl/index.html> (B. Bischl); <https://cmutschler.de/> (C. Mutschler)

ORCID(s): 0000-0002-4392-0830 (F. Ott); 0000-0001-6670-3698 (L. Heublein); 0000-0002-8772-9202 (D. Rügamer); 0000-0001-6002-6980 (B. Bischl); 0000-0001-8108-0230 (C. Mutschler)

🌐 <https://www.linkedin.com/profile/view?id=felix-ott-494b06146> (F. Ott), <https://www.linkedin.com/profile/view?id=david-ruegamer> (D. Rügamer), <https://www.linkedin.com/profile/view?id=christopher-mutschler-28431576> (C. Mutschler)

Each method for absolute pose prediction, including SfM, APR, and RPR, has its own drawbacks, and each pose is affected by different sources of noise, as highlighted by Sattler et al. (2019). APR algorithms such as PoseNet (Kendall et al., 2015) learn a set of base poses such that the poses of all training images can be expressed as a linear combination of these base poses. The base translations estimated by PoseNet are significantly more noisy than those by SfM and do not all align on a straight line. Hence, PoseNet is still not able to generalize well across different scenarios Sattler et al. (2019). To improve the performance of these methods, it is desirable to combine absolute poses (from SfM or APR) and relative poses (through RPR from optical flow). The motivation for fusing absolute and relative pose methods lies in addressing the limitations and enhancing the robustness of pose estimation systems: (1) Utilizing complementary information, i.e., APR methods provide global positioning but may suffer from long-term drift over time, while RPR methods excel in short-term accuracy but lack a global reference. By combining both approaches, the strengths of each can be leveraged, compensating for the weaknesses and creating a more reliable and accurate overall pose estimation (Huang et al., 2011). (2) Integrating relative pose information allows for periodic correction, mitigating the effects of drift and enhancing long-term accuracy (Fuentes-Pacheco et al., 2012). (3) APR methods may struggle in dynamic or complex environments where changes occur rapidly. By incorporating relative pose information, the system's adaptability to local changes is enhanced (Barros et al., 2022). (4) A fusion of absolute and relative pose methods creates a hybrid system that can be adaptable to various applications and scenarios. (5) Methods that utilize multiple sensors with different strengths and weaknesses can be improved by fusing absolute and relative pose information (Kazerouni et al., 2022). While some approaches combine both fields or different modalities by a common representation between networks (Ott et al., 2022a; Brieger et al., 2022), others directly combine the absolute and relative poses (Mitsuki et al., 2021). However, fusing absolute and relative poses is a challenging task since RPR requires knowledge of the global pose, which may contain errors. Pose graph optimization (PGO) (Brahmbhatt et al., 2018; Mirowski et al., 2018) is a technique that estimates smooth and globally consistent pose predictions during inference. Another approach is to use a fusion module based on recurrent cells (Ott et al., 2020), which can learn an improved (i.e., smoothed), long-term trajectory, but requires time-distributions (i.e., applies a layer to every temporal slice of an input) to learn the orientation of the relative to the global pose. Despite recent advances, optimizing the absolute pose with neural networks remains an open research topic.

Another research goal of visual self-localization is to develop methods that can adapt to new and unknown scenes or remain robust to environmental changes (Idan et al., 2023; Winkelbauer et al., 2021; Wang and Qi, 2023; Acharya et al., 2023), such as adding or removing racks in warehouses. To achieve this, some approaches use multi-scene

APR techniques (e.g., employing Transformers) to learn multiple scenes simultaneously (Shavit et al., 2022), use auto-encoders (Shavit and Keller, 2022), or apply transfer learning between different scenes (Chidlovskii and Sadek, 2021). To improve the performance of the initial weights, we pre-train the APR and RPR models using synthetic data.

Contributions. The primary objective of this work is to optimize the accuracy of absolute poses by fusing absolute and relative poses. To achieve this goal, the following steps are taken: (1) To enhance the performance of SfM in retrieving absolute poses, we conduct a large hyperparameter search. PoseNet (Kendall et al., 2015) is alternatively evaluated as an APR technique. The relative poses are regressed from optical flow computed with the Lucas-Kanade (Baker and Matthews, 2004) algorithm. The objective is to use these techniques as baseline black box models and focus on the optimization of fusion methods. (2) We evaluate PGO (Mirowski et al., 2018) to optimize the pose and conduct a benchmark to assess the performance of eight recurrent and 17 convolutional, recurrent, and Transformer networks in absolute and relative pose fusion. (3) As there is currently no publicly available dataset to evaluate large-scale challenging environments, we record and publish¹ a large database containing various scenes with changes between scenes. This dataset is used to conduct experiments assessing the robustness of methods against volatile environments. (4) We develop a simulation framework to generate and pre-train the APR and RPR models on synthetic data. Advanced techniques may be used as black box models in place of the baseline models (SfM, APR, RPR) to further enhance the results. However, the focus of this study is on assessing the performance of the fusion techniques with respect to environmental changes and motion dynamics on the localization task.

The remainder of this article is organized as follows. We discuss related work in Section 2. Section 3 introduces our method, including SfM, APR, RPR, and fusion modules. We present novel datasets and our simulation for data generation in Section 4, and discuss experimental results in Section 5.

2. Related Work

The fields of SfM and APR have experienced significant growth in recent years, resulting in a broad and diverse body of research. This work, however, primarily focuses on fusing absolute and relative poses. For a comprehensive overview of SfM approaches, please refer to Jiang et al. (2020); Zheng et al. (2018); Piasco et al. (2018); Brachmann et al. (2023); Radanovic et al. (2023). For a detailed review of APR techniques, see Sattler et al. (2019); Ott et al. (2022a); Xu et al. (2022); Blanton (2021); Qiao et al. (2023). An overview of APR loss functions can be found in Boittiaux et al. (2022); Pepe and Lasenby (2023). In Section 2.1, we introduce techniques for RPR estimation using optical flow. State-of-the-art techniques for fusing absolute and relative

¹Datasets and source code: https://gitlab.cc-asp.fraunhofer.de/ottf/industry_datasets

poses are discussed in Section 2.2, while Section 2.3 presents related work on scene generalization through simulation.

2.1. RPR from Optical Flow

Numerous techniques exist for estimating the relative pose from successive image pairs by utilizing optical flow, including Flowdometry (Muller and Savakis, 2017; Muller et al., 2016), ViPR (Ott et al., 2020), DeepVIO (Han et al., 2019), KFNet (Zhou et al., 2020), and the model by Ott et al. (2022a). These methods employ either FlowNet or FlowNet-Simple by Dosovitskiy et al. (2015) or FlowNet2 (Ilg et al., 2017) for estimating optical flow. While LS-VO (Costante and Ciarfuglia, 2018) uses an autoencoder to predict optical flow and estimate a trajectory from a neural network, we compute the optical flow using the Lucas-Kanade (Baker and Matthews, 2004) algorithm. In contrast, Zhi-Yu et al. (2021) utilizes the relative pose as auxiliary information for optical flow prediction of FlowNet2. Our method uses the Lucas-Kanade (Baker and Matthews, 2004) algorithm in combination with a small relative model. DeepVO (Wang et al., 2017), CTCNet (Iyer et al., 2018), DistanceNet (Kreuzig et al., 2019), and MotionNet (Ding et al., 2020) do not rely on optical flow but combine CNNs with RNNs, such as stacked LSTMs, bidirectional LSTMs, or fully connected layers, to model sequential dynamics and relationships to predict relative poses. Similarly, our relative model consists of convolutional layer in combination with LSTMs. Muller and Smith (2023) use pretrained semantic segmentation and optical flow to extract ground plane correspondences between aligned images and RANSAC to find the best fitting homography. In contrast, DiffPoseNet (Parameshwara et al., 2022) uses normal flow to estimate relative camera pose based on the cheirality (depth positivity) constraint by formulating a optimization problem as a differentiable layer. While DiffPoseNet uses flow to improve the coarse absolute predictions from PoseNet, our model directly predicts the relative poses to refine the absolute poses.

2.2. APR & RPR Fusion

LM-Reloc (von Stumberg et al., 2020) formulates its loss based on the Levenberg-Marquardt algorithm to improve direct image alignment through learned features. It also incorporates an RPR model to bootstrap the direct image alignment. ViPR (Ott et al., 2020) enhances absolute poses by concatenating relative poses predicted from optical flow and absolute poses, and then refining them using an LSTM network. MapNet+PGO (Brahmbhatt et al., 2018) refines predicted poses from APR and RPR using PGO. VLocNet (Valada et al., 2018) estimates global poses and combines it with VO, while VLocNet++ (Radwan et al., 2018) adds features from semantic segmentation. RCNN (Lin et al., 2019) fuses relative and global sub-networks to smooth VO and prevent drift. Mitsuki et al. (2021) propose a graph neural network that uses image-to-nodes and image-to-edges to create similarity-preserving mappings, with nodes representing absolute features and edges representing relative features. Kalman filters are frequently employed for pose fusion, such as in the work by Emter

et al. (2019). This approach combines absolute and relative measurements, leading to a correlation between a past state and present state that creates correlations. Our objective is to mitigate these correlations by utilizing an optimal recurrent cell. In general, LSTM cells are employed for representing temporal dependencies in localization tasks. Recently, Transformer networks have been applied in visual self-localization, as demonstrated by the methods proposed by Shavit et al. (2022); Li and Ling (2022); Kim and Kim (2023); Li et al. (2023a). Nevertheless, Transformers are not well-suited for integrating absolute and relative poses due to their low-dimensional information. Additionally, the bidirectional properties (Graves et al., 2009) of LSTMs are deemed unfeasible for pose modeling. Ruan et al. (2023) fuse APR with scene coordinate regression. While Lu and Lu (2019) combine a depth map from a single-view depth network with relative poses from a pose network, Yang et al. (2020) proposed D3VO that combines the depth map with relative poses from PoseNet. In contrast, Zhan et al. (2020) proposed the combination of a depth network with optical flow. However, this method is designed solely for visual odometry. Li et al. (2021) independently utilize a depth network, optical flow network, and camera motion network, which are jointly optimized during the training phase. The objective is to predict various masks by combining four types of loss functions specifically for relative prediction.

Das and Dubbelman (2018) fuse absolute poses derived from GNSS data with relative poses obtained from vehicle odometry. Two subsequent works integrate relative poses from inertial data with absolute poses from visual data. VINet (Clark et al., 2017) uses a concatenation approach to merge relative features, extracted by an inertial LSTM encoder, with absolute features, extracted by a visual encoder. In contrast, VI-DSO (von Stumberg et al., 2018) employs a combined energy functional to jointly estimate camera poses and sparse scene geometry by minimizing both visual and inertial measurement errors.

A related yet distinct field is depth estimation, which is also employed in APR and RPR techniques. Research in this area often emphasizes self-supervised learning (Godard et al., 2019), diffusion models (Saxena et al., 2023) due to recent advancements, and Transformer architectures (Zhang et al., 2023). Many additional depth estimation techniques are available and could be integrated into fusion methods, albeit not within the context of SfM and RPR methods.

2.3. Simulation for Scene Generalization

Today's regression-based techniques for APR are scene-specific with respect to their training and evaluation. They rely on the coordinate system of the training dataset, leading to poor generalization across different scenes (Chidlovskii and Sadek, 2021). The Transformer network, proposed by Shavit et al. (2022), learns multi-scene APR. The model employs encoders to aggregate activation maps via self-attention and decoders to transform latent features and

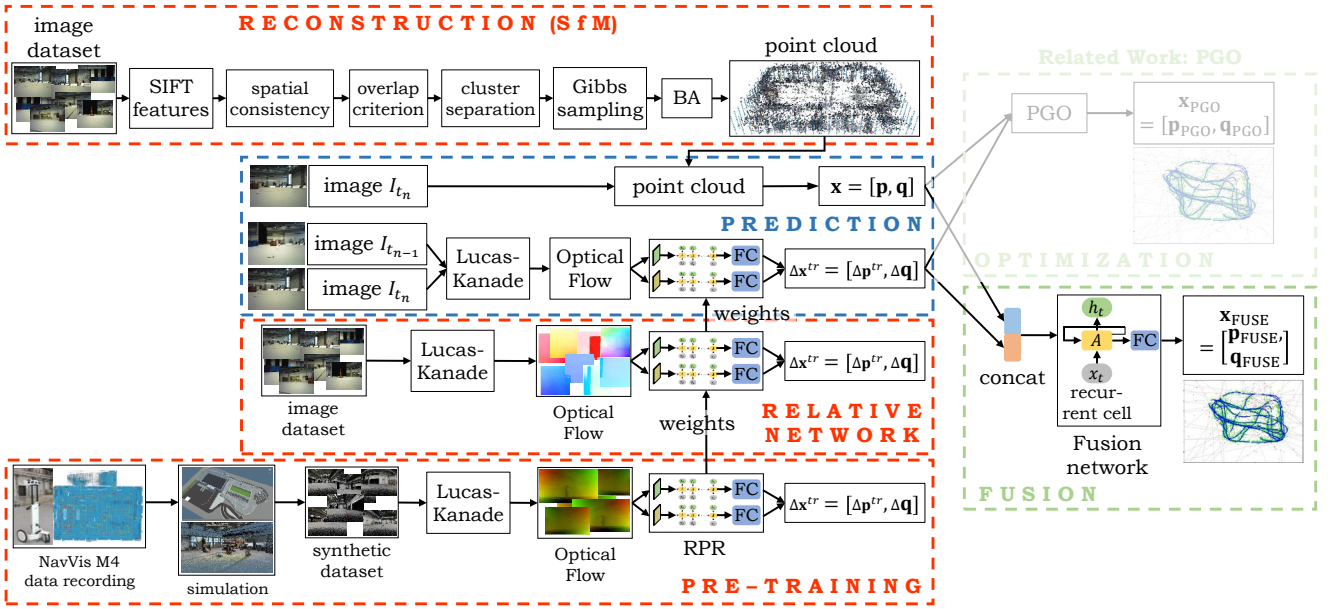


Figure 1: Method overview. First, a point cloud is constructed from an image dataset using SfM to extract features, spatial consistency, overlap criterion, cluster sampling, and bundle adjustment (BA). Second, we train a small convolutional recurrent neural network to predict the relative pose Δx between two consecutive images. For the training of the fusion model and the evaluation step, the absolute pose x from the point cloud and the relative pose Δx^{tr} from the RPR model is retrieved for a query image. Last the absolute pose is optimized with either PGO or a recurrent network. To compare with state-of-the-art methods, we replace the reconstruction and the point cloud in the prediction steps with the absolute pose prediction from the APR model.

scenes encoding into predicted pose. This approach allows the model to learn informative features while embedding multiple scenes in parallel. To address the issue of dataset shift, Chidlovskii and Sadek (2021) developed a deep adaptation network that can learn scene-invariant image representations for transfer learning. Furthermore, Chidlovskii and Sadek (2021) use adversarial learning to generate such representations for the model transfer. Wang and Qi (2023) report that single-input images can cause confusion in relocalization when dealing with scenes that share similar views but differ in position, which motivates the use of a time-distributed network. Furthermore, they highlight the difficulty of relocalization in variable or dynamic scenes. Wang and Qi (2023) created a variable scene dataset comprising three scenes: an office, a bedroom, and a sitting room. They use semi-automatic processing to develop their MMLNet method, which can regress both camera pose and scene point cloud. Similarly, our approach involves the fusion of point clouds and relative poses. Acharya et al. (2023) uses a generative network to model fake synthetic images for APR.

While APR techniques learn absolute scene parameters, RPR methods can localize in unseen environments by learning the residual pose between image pairs. However, RPR methods often perform poorly in unfamiliar scenes. To improve the generalization of RPR methods, Idan et al. (2023) enhanced their performance by aggregating paired feature maps into latent codes. Additionally, Winkelbauer et al. (2021) proposed an RPR approach based on ResNet that includes changes to the model architecture, such as an

extended regression part, hierarchical correlation layers, and the incorporation of uncertainty and scale information, to better generalize to new scenes.

In summary, prior works have focused on incorporating auxiliary information into models to learn both general features and scene-specific features that can generalize across various scenes. However, no existing approach learns scene information from simulated environments (absolute) or motion from simulated dynamics (relative) (Idan et al., 2023; Winkelbauer et al., 2021; Shavit et al., 2022).

3. Methodology

Firstly, we present the reconstruction of a point cloud from an image dataset using SfM (see Section 3.1). Section 3.2 describes an alternative approach based on APR. The Lucas-Kanade method for computing optical flow and our RPR network are presented in Section 3.3. Description of absolute and relative pose fusion is provided based on these APR and RPR methods. Furthermore, we evaluate PGO in Section 3.4 and propose a framework of models that utilize various RNNs in Section 3.5. Finally, in Section 3.6, we discuss the rationale for pre-training APR and RPR to improve generalizability to various scenarios. Figure 1 presents an overview of the method, illustrating all steps.

3.1. Structure from Motion

This section outlines the steps involved in using SfM to create a point cloud. The SfM pipeline is proposed in Figure 2, while Table 1 provides a summary of the hyperparameters used in each step.

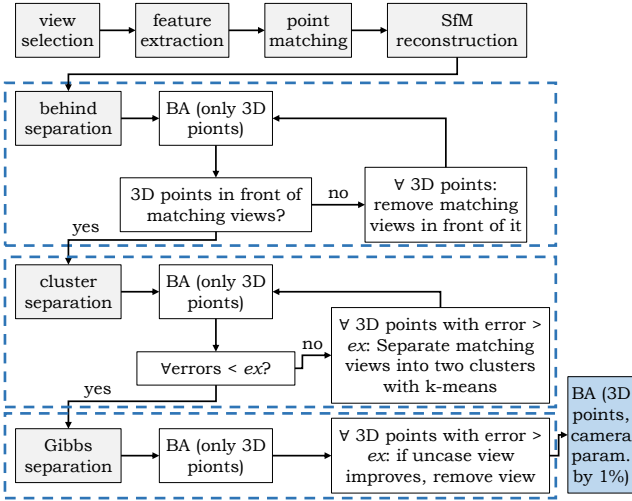


Figure 2: SfM pipeline using bundle adjustment (BA) to reconstruct a point cloud from input images.

SfM. We adopt the source code provided by Venkataraman (2020) as the baseline for our SfM pipeline, which is used to recover 3D structure of a given environment. SfM is employed to determine the relative pose of each image with respect to the first image. Inspired by the findings of Resch et al. (2015), which suggest using every fifth image for reconstruction, we manually pre-select around 600 images from each dataset (comprising between 7,000 to 138,000 images) for point cloud reconstruction. Additionally, we obtain the intrinsic matrix, essential for recalibration, by capturing images of a checkerboard using our camera setup. For the sake of reproducibility, we report the following calibration matrix:

$$K = \begin{bmatrix} 548.44934818 & 0.0 & 317.73762648 \\ 0.0 & 540.17600512 & 249.00614224 \\ 0.0 & 0.0 & 1.0 \end{bmatrix} \quad (1)$$

We ensure to avoid matching two points from the same image with a single point from the point cloud.

Feature Extraction. We utilize the opencv-python cv2 library (OpenCV, 2022) to extract image features, which yields descriptors of size 128 for each image. In a pre-defined study, we assess the impact of three feature extraction techniques, namely, scale-invariant feature transform (SIFT) proposed by Lowe (2004), speeded up robust features (SURF) introduced by Bay et al. (2006), and oriented fast and rotated brief (ORB) proposed by Rublee et al. (2011), on the reconstruction performance. Based on our evaluation, we select SIFT as the feature extraction technique for our pipeline.

Spatial Consistency & Overlap Criterion. In addition, we employ spatial consistency to enhance the discriminative capability of the raw feature points by evaluating the matching quality of feature points in a larger spatial neighborhood.

Table 1

Overview of SfM hyperparameters.

Parameter	Description
<i>sc</i>	Spatial consistency of the point neighborhood in pixel
<i>oc</i>	Overlap criterion of floor pixels between images in %
<i>mm</i>	Minimal number of matches for each point over all images
<i>ex</i>	Exclude points with reprojection error larger than separation limit in pixel
<i>gibbs</i>	Boolean of <i>gibbs</i> factor of pixel improvement by excluding single points
<i>std</i>	Standard deviation for point exclusion for BA

We follow the approach proposed in Jiang et al. (2020), which involves computing the ratios of features that fall into two corresponding regions. We introduce a hyperparameter *sc* that specifies the spatial consistency of the point neighborhood in terms of the number of pixels. We also apply an overlap criterion to filter out unnecessary image pairs. We divide the ground floor into a grid and require each image to contain a specific percentage (controlled by the parameter *oc*) from these grid points.

Cluster Separation. Points from multiple images can correspond to the same point in the point cloud. To handle such cases, we partition these image points into clusters and explore the possibility of improving the match separation, as proposed in Jiang et al. (2020). This results in the creation of additional clusters in the point cloud. We use the hyperparameter *mm* to determine the number of matches. For neighborhood clustering, we use k-means with two clusters. We apply this strategy iteratively with bundle adjustment (BA) until the hyperparameter *ex* falls below a predefined threshold in terms of pixels.

Gibbs Sampling. We first apply BA. Next, we iterate through all image points for each point in the point cloud. We employ Gibbs sampling to iteratively remove one point from the selected image points and evaluate whether the remaining points improve the performance of the BA. We adjust the hyperparameter *gibbs* for this process.

Bundle Adjustment. We adopt the sparse BA method proposed in Github (jahdiel) (2016). Additionally, we define parameters to regularize the point cloud to remain within the environment. In all BA steps, we keep the rotation matrix fixed, and only change the rotation matrix of the last BA step. We tune the hyperparameter *std*, which represents the standard deviation for point exclusions.

3.2. Absolute Pose Regression

In order to reduce the computational requirements associated with hyperparameter tuning for SfM (provided in Section 5.1), an alternative approach involves using APR methods, as discussed in Section 2.2. Rather than tuning

hyperparameters, a CNN-based APR model can learn to directly regress the camera pose from a single input image in conjunction with their corresponding ground truth poses. In our case, we utilize a time-distributed network that takes a set of three consecutive images as input (at timesteps t_{n-2} , t_{n-1} , and t_n) to predict absolute positions $\mathbf{p} \in \mathbb{R}^3$ in Euclidean coordinates and absolute orientations $\mathbf{q} \in \mathbb{R}^4$ as quaternions of the absolute pose $\mathbf{x} = [\mathbf{p}, \mathbf{q}]$. We use the PoseNet architecture (Kendall et al., 2015) based on GoogLeNet (Szegedy et al., 2015) with time-distribution (Ott et al., 2020). Our network includes a fully connected (FC) layer of 2,048 units, and two parallel FC layers, each with three and four units. We minimize the root mean squared error (RMSE) loss function

$$\mathcal{L}_{\text{APR}} = \|\hat{\mathbf{p}} - \mathbf{p}\|_2^2 + \beta_1 \left\| \hat{\mathbf{q}} - \frac{\mathbf{q}}{\|\mathbf{q}\|_2} \right\|_2^2, \quad (2)$$

between the predicted pose $\mathbf{x} = [\mathbf{p}, \mathbf{q}]$ and ground truth pose $\hat{\mathbf{x}} = [\hat{\mathbf{p}}, \hat{\mathbf{q}}]$, weighted by the hyperparameter $\beta_1 = 50$. We use a batch size of 50, the Adam optimizer without decay, and a learning rate of 10^{-4} .

3.3. Relative Pose Regression from Optical Flow

We utilize the Lucas-Kanade (Baker and Matthews, 2004) algorithm to compute the optical flow between two images captured at timesteps t_{n-1} and t_n for learning the relative movements and rotations of an object. Optical flow is a vector field representation of the movement of objects or surfaces in a sequence of images or video, as captured by a camera. Each vector in the optical flow field corresponds to the displacement of a small portion of the image from frame t_{n-1} to frame t_n . Hence, we receive the pixel movements in u and v direction. The Lucas-Kanade algorithm is a classic differential method that assumes uniform motion of objects in a small local neighborhood and solves a system of linear equations relating the spatial and temporal derivatives of the image intensity to the local motion parameters. We present an exemplary visualization of optical flow in Figure 3.

We propose the following recurrent network for the purpose of regressing the relative pose from optical flow. To achieve this, we initially subject the vector input, which has a size of $480 \times 640 \times 2$ pixels, to 4×4 mean average pooling with stride 1, resulting in a tensor size of $120 \times 160 \times 2$. In this case, u and v represent the third dimension of the optical flow. We then proceed to search for an optimal network configuration, which may involve batch normalization, adding one or two stacked LSTM layer, and ReLU, softmax, or no activation. Our chosen network configuration involves the absence of batch normalization and activation, and the use of one LSTM layer with 50 units for each direction of u and v by slicing the third dimension of the optical flow. The output of the LSTM layers is then concatenated, and two FC layers of size 3 and 4 are added to predict the relative pose $\Delta \mathbf{x} = [\Delta \mathbf{p}^{lr}, \Delta \mathbf{q}]$, i.e., the relative position (translation) $\Delta \mathbf{p}^{lr} \in \mathbb{R}^3$ and the relative orientation (rotation) $\Delta \mathbf{q} \in \mathbb{R}^4$. To minimize error, we apply a mean squared error (MSE) loss function

$$\mathcal{L}_{\text{RPR}} = \|\Delta \hat{\mathbf{p}}^{lr} - \Delta \mathbf{p}^{lr}\|_2 + \beta_2 \left\| \Delta \hat{\mathbf{q}} - \frac{\Delta \mathbf{q}}{\|\Delta \mathbf{q}\|_2} \right\|_2, \quad (3)$$

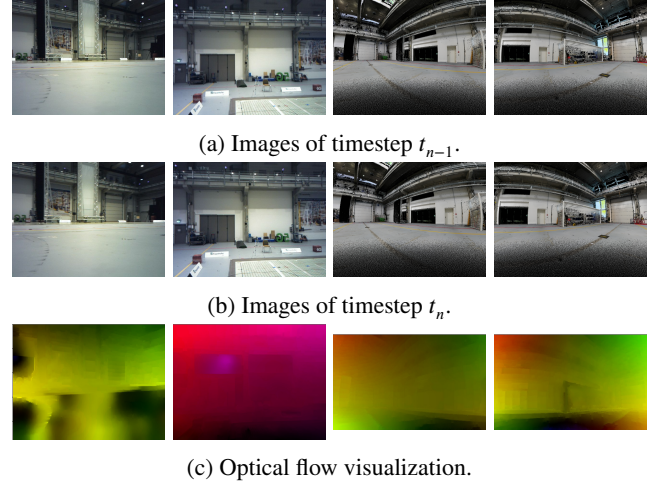


Figure 3: Exemplary optical flow visualizations (c) between two consecutive images (a and b) of real-world scenarios (image 1 and 2) and simulated scenarios (image 3 and 4). Note the small movement between timestep t_{n-1} (a) and timestep t_n (b).

with the ground truth relative pose $\Delta \hat{\mathbf{x}} = [\Delta \hat{\mathbf{p}}^{lr}, \Delta \hat{\mathbf{q}}]$. Therefore, we transform the global coordinate systems of consecutive cameras to a local coordinate system $\bar{\mathbf{p}} = \mathbf{R}\mathbf{p}$ with the rotation matrix \mathbf{R} , such that $\mathbf{R}^T = \mathbf{R}^{-1}$ and $\mathbf{R}^T \mathbf{R} = \mathbf{R}\mathbf{R}^T = \mathbf{I}$. The relative poses $\Delta \mathbf{p}^{lr}$ represent the differences between the rotated poses. We weight the orientational loss function with $\beta_2 = 50$. Additionally, we use a batch size of 50, the Adam optimizer without decay, and a learning rate of 10^{-4} . Finally, the relative ground truth labels are transformed based on the current orientation of the absolute pose.

3.4. Pose Graph Optimization

We employ the PGO algorithm (Mirowski et al., 2018) as the state-of-the-art method for fusing absolute and relative poses, which provides smooth and globally consistent pose estimates. PGO can be formulated as a non-convex minimization problem represented by a graph with vertices corresponding to the estimated global poses and edges representing the relative poses. The goal is to ensure that the refined relative poses align with the input relative poses (Brahmbhatt et al., 2018; Ott et al., 2022a). To reduce runtime complexity, we split the absolute and relative poses into 100-sample chunks with a 20-sample overlap. We conducted a search for the optimal parameters that results in the lowest positioning error.

3.5. APR-RPR Fusion based on Recurrent Cells

Our contribution is a recurrent model for fusing absolute and relative poses to achieve a smoother absolute pose estimation and optimize localization error. To accomplish this, we concatenate the output pose of the absolute method (refer to Section 3.1 and Section 3.2) of size $(N_t \times BS \times 7)$ and the output pose of the relative method (refer to Section 3.3) of size $(N_t \times BS \times 7)$, resulting in a network input of size $(N_t \times BS \times 14)$, where N_t is the number of timesteps and

BS is the batch size. The objective is to predict an improved absolute pose at timestep t_n from the concatenated absolute and relative poses of timesteps $\{t_{n-N_t-1}, \dots, t_n\}$. For pose refinement, we implement the following recurrent network, which includes one or two stacked RNN cells. The output size of the first cell is $(N_t \times BS \times 14)$, while the output size of the second cell is $(BS \times r_u)$, where r_u represents the number of units in the RNN cell. Finally, we include two FC layers, similar to the APR model (refer to Section 3.2), with the RMSE loss function

$$\mathcal{L}_{\text{APR-RPR}} = \|\hat{\mathbf{p}} - \mathbf{p}\|_2^2 + \beta_3 \left\| \hat{\mathbf{q}} - \frac{\mathbf{q}}{\|\mathbf{q}\|_2} \right\|_2^2, \quad (4)$$

and weighting $\beta_3 = 50$, a batch size of 100, the Adam optimizer without decay, and a learning rate of 10^{-4} . In Section 5.4, we present a hyperparameter search for N_t , r_u , and the number of stacked recurrent cells (one or two).

The vanishing gradient problem is a major issue with RNNs, which occurs when gradients become too small as they propagate backwards through time during weight updates. This can be problematic in our fusion model due to small orientation entries (i.e., quaternions with magnitudes below 1), hindering the learning of long-term dependencies. To address this issue, we explore various recurrent cells that can allow the model to learn the dynamics of an object (i.e., slow moving robot versus fast moving human) on the low-level pose representation. Object movements typically follow predictable, non-chaotic patterns that follow physical behavior (Ott et al., 2022b). One solution is to use gating mechanisms such as those found in long short-term memory (LSTM) (Hochreiter and Schmidhuber, 1997) and gated recurrent unit (GRU) (Chung et al., 2014). Another option is the minimal gated unit (MGU) (Zhou et al., 2016; Heck and Salem, 2017), which is a simplified version of LSTM and GRU that uses only an update and reset gate. The recurrent additive network (RAN) (Lee et al., 2017) is another type of gates RNN that uses purely additive latent state updates. For greater parallelism, we evaluate the simple recurrent unit (SRU) (Lei et al., 2017), which simplifies computations as the majority of computations for each step are independent of recurrence. Additionally, quasi-recurrent neural networks (QRNN) (Bradbury et al., 2017) apply minimalistic recurrent pooling functions in parallel across channels. Balduzzi and Ghifary (2017) proposed strongly-typed RNN (TRNN), which learns simple semantic interpretations via dynamic average pooling. The chaos free network (CFN), proposed by Laurent and von Brecht (2017), is a type of RNN that models non-chaotic dynamics.

Furthermore, we evaluate convolutional networks, such as FCN (Wang et al., 2016), TCN (Bai et al., 2018), ResNet (Wang et al., 2016), ResCNN (Zou et al., 2019), Inception-Time (Fawaz et al., 2020), XceptionTime (Rahimian et al., 2019), and OmniScaleCNN (Tang et al., 2022), a combination of recurrent with fully convolutional networks, i.e., LSTM-FCN (Karim et al., 2017), GRU-FCN (Elsayed et al., 2019), and MLSTM-FCN (Karim et al., 2019), Transformer models, i.e., TST (Zerveas et al., 2021), TSPerceiver (Jaegle

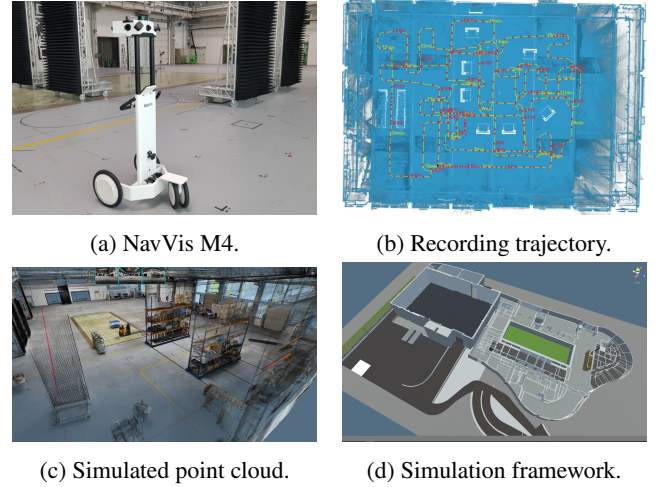


Figure 4: Creation of simulated images for pre-training.

et al., 2021), and TSSequencerPlus (Tatsunmai and Taki, 2022), as well as mWDN (Wang et al., 2018), XCM (Fauvel et al., 2022), and gMLP (Liu et al., 2021).

3.6. Simulation-Augmented Pre-Training

Pre-training neural networks using simulated data can enhance their performance in various tasks, especially in the case of data scarcity, domain adaptation, data augmentation, and providing a good initialization for transfer learning to real data (Zhang et al., 2017; Shrivastava et al., 2017). Previous studies in the context of visual self-localization (Winkelbauer et al., 2021; Idan et al., 2023; Wang and Qi, 2023) have demonstrated the potential benefits of pre-training on synthetic data for improved performance. To this end, we develop a simulation environment with a loaded point cloud of the real-world environment to generate a large number of samples and augment the APR and RPR models for better initial weights, improved adaptability to unseen scenarios, and enhanced transfer learning to changes in the environment. Figure 4 illustrates the data generation process. Initially, we record a large dataset using a NavVis M4 system (see Figure 4a) while moving in an environment with seven large black absorber walls and two warehouse racks, as shown in Figure 4b. Next, we create a detailed point cloud (see Figure 4c) from this dataset, which was then loaded into the simulation framework implemented by Shhuna GmbH (see Figure 4d). We only use the large hall of the simulation framework (left part) for data generation. Using a fish-eye camera (in the simulation), we generated 319,955 images mimicking a slow moving robot, see Figure 3 (third and fourth column) for exemplary images. We concurrently capture images from three cameras, including one front-facing camera and two side-facing cameras. We utilized this dataset to pre-train the APR and RPR models on a large dataset.

Table 2

Overview of the visual Industry scenario #4 datasets recorded in a large-scale indoor environment with a robot or handheld.

Dataset	Setup	# Images
Train 1	Robot, clear environment	92,668
Train 2	Robot, four absorber walls with objects	19,872
Train 3	Robot, four absorber walls	138,233
Train 4	Handheld, person 1, four absorber walls	27,856
Train 5	Handheld, person 2, four absorber walls	28,113
Train 6	Robot, open environment with objects	114,998
Train 7	Robot, open environment with objects and labyrinth	29,240
Train 8	Robot, open environment with object, labyrinth, and absorber walls	110,923
Test 1	Robot, clear environment	23,168
Test 2	Robot, one absorber wall	30,379
Test 3	Robot, two absorber walls	24,752
Test 4	Robot, three absorber walls	26,877
Test 5	Robot, four absorber walls with objects	4,968
Test 6	Robot, four absorber walls	34,559
Test 7	Handheld, person 1, four absorber walls	6,964
Test 8	Handheld, person 2, four absorber walls	7,029
Test 9	Robot, open environment with objects	28,750
Test 10	Robot, open environment with objects and labyrinth	7,311
Test 11	Robot, open environment with objects, labyrinth, and absorber walls	27,732

4. Experiments

In the following section, we provide details regarding the data collection and experiments. Specifically, Section 4.1 offers an overview of our datasets and the challenges associated with localization. Section 4.2 provides a summary of our experiments. Finally, in Section 4.3, we describe the hardware setup and evaluation metrics used in our study.

4.1. Datasets & Challenges

Numerous datasets are currently accessible for assessing APR techniques. Nevertheless, the present datasets possess limitations such as being captured outside the industrial environments or with equipment such as micro aerial vehicles (MAVs) or handheld devices, or are inadequate for evaluating specific scenarios like changes in the environment. Therefore, we have captured the Industry dataset in a vast large-scale industrial environment covering an area of $1,320m^2$, similar to the environment in Löffler et al. (2018); Ott et al. (2020, 2022a); Stahlke et al. (2022). A small robotic recording platform is constructed, equipped with an Orbbec3D camera featuring an RGB image resolution of 640×480 pixels and a recording frequency of 23 Hz. To measure reference poses at a high-precision level ($< 1mm$), a motion capture system operating at 140 Hz is utilized. Eight training and 11 testing datasets are recorded, comprising 10 distinct scenarios, as presented in Table 2. Trajectories are depicted in Figure 6. Changes are introduced to the environment between recordings to assess the model’s robustness against volatile objects, i.e., the removal or addition of absorber walls, and the ability to generalize and adapt to various scenarios and motion dynamics. Initially, a large-scale clear environment without objects was recorded.

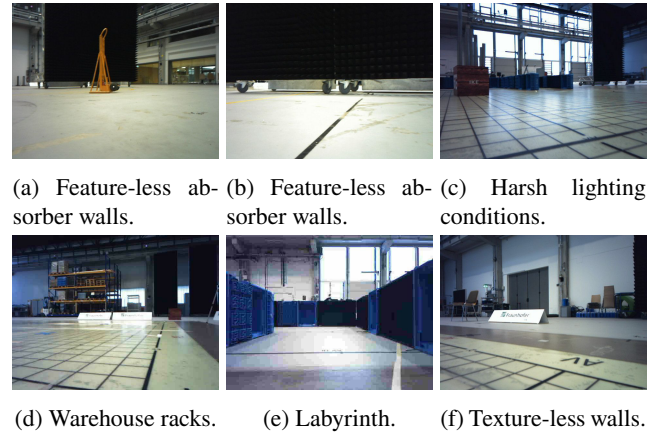


Figure 5: Exemplary challenging images of the large-scale indoor environment.

Subsequently, we introduced one, two, three, or four absorber walls, along with smaller objects. Additionally, a small “labyrinth” in an L-like configuration was constructed, as shown in Figure 6g and Figure 6r. Finally, we captured the motion dynamics of two individuals randomly walking in the environment, with four absorber walls present (see trajectories in Figure 6d, 6e, 6o, and 6p).

The motion dynamics between the robot and humans are different. Cross-validation is conducted for all training and test datasets. Figure 5 presents images that are challenging with respect to the localization task, including the feature-less structure of the absorber walls (Figure 5a and Figure 5b), which makes it particularly hard for SfM to extract features and match image points, or different scalings between distant warehouse racks (Figure 5d) and the small-scale labyrinth

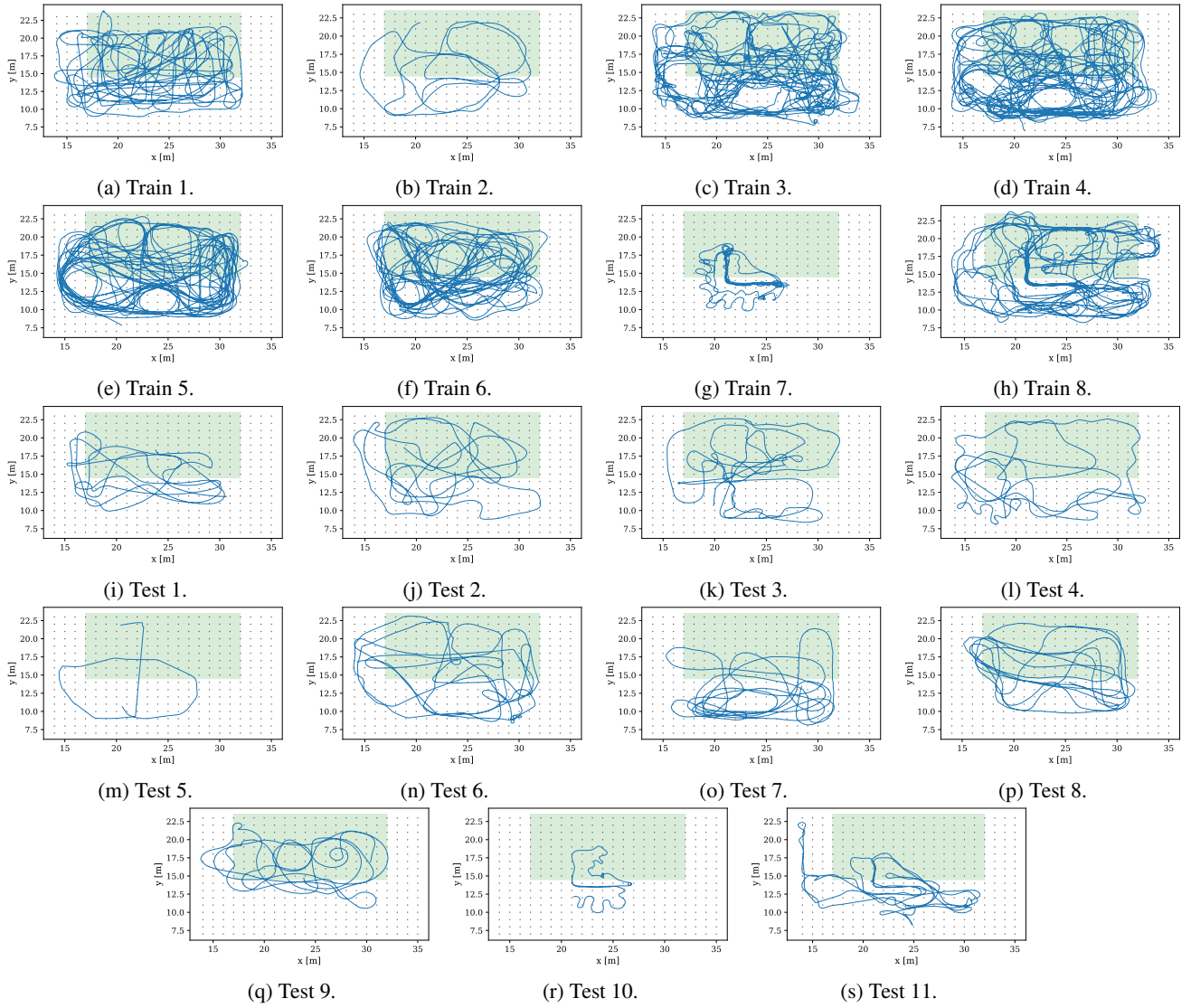


Figure 6: Trajectories of the Industry datasets with $x \in [14, 34]$ and $y \in [7, 23]$.

(Figure 5e). See Zangeneh et al. (2023), for challenges under ambiguous scenes.

4.2. Overview of Experiments

Table 3 provides a comprehensive summary of the experiments conducted in our study. Our approach to estimating absolute pose involves either applying SfM (see Section 3.1) or using the time-distributed APR model (see Section 3.2). To predict relative poses, we utilize the RPR model (see Section 3.3). We evaluate the performance of both APR and RPR models with and without pre-training on the synthetically generated dataset (see Section 3.6). In terms of fusion, we compare our proposed fusion framework with eight different recurrent cells, namely LSTM, GRU, MGU, RAN, SRU, QRNN, TRNN, and CFN (see Section 3.5), against the state-of-the-art PGO technique (see Section 3.4).

Table 3

Overview of different fusion combinations.

Absolute Pose	Relative Pose	Fusion
SfM	RPR	PGO
SfM	RPR (pre-trained)	PGO
APR	RPR	PGO
APR	RPR (pre-trained)	PGO
APR (pre-trained)	RPR	PGO
APR (pre-trained)	RPR (pre-trained)	PGO
SfM	RPR	Recurrent model
SfM	RPR (pre-trained)	Recurrent model
APR	RPR	Recurrent model
APR	RPR (pre-trained)	Recurrent model
APR (pre-trained)	RPR	Recurrent model
APR (pre-trained)	RPR (pre-trained)	Recurrent model

4.3. Hardware Setup & Evaluation Metrics

For all experiments, we use Nvidia Tesla V100-SXM2 GPUs with 32 GB VRAM equipped with Core Xeon CPUs and 192 GB RAM. We use the Adam optimizer with a

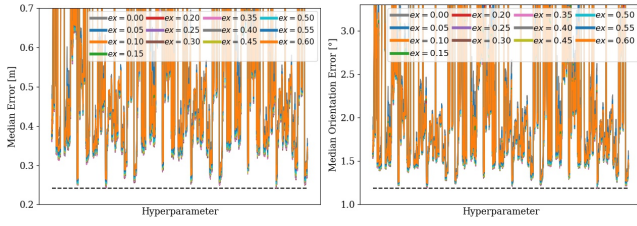

 (a) Median position error in m . (b) Median orientation error in $^\circ$.

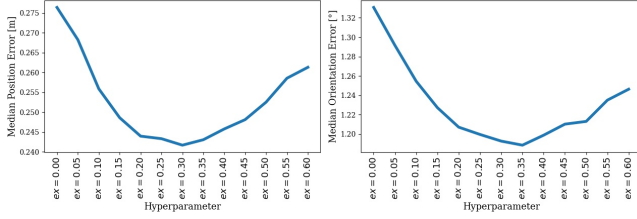
Figure 7: Evaluation of all SfM point clouds (for different hyperparameters, see x-axis) for the robot train 3 and test 6 datasets. The dashed lines indicate the lowest error.

 (a) Median position error in m . (b) Median orientation error in $^\circ$.

Figure 8: Evaluation of the best SfM point cloud (from Figure 7) for different hyperparameters *exclude* for the robot train 3 and test 6 datasets.

learning rate of 10^{-4} . We run each experiment for epochs = (iterations \cdot BS)/dataset_size, where we set iterations to 150,000 for APR and RPR and to 75,000 for the fusion models, the batch size BS is 50 for APR and RPR and 100 for the fusion models, and the dataset size depends on the scenario according to Table 2. We report results for the last epoch. For the evaluation of absolute predictions, we report the median absolute position in m and the median absolute orientation in $^\circ$.

The network framework proposed in this paper comprises multiple training stages. Initially, the dataset undergoes recording and pre-processing procedures. Subsequently, the SfM algorithm is employed to construct a point cloud, facilitating the computation of absolute poses from testing images. Additionally, the RPR network is trained on optical flow images generated using the Lucas-Kanade algorithm. The RPR network predicts relative poses between pairs of consecutive images. Finally, the third network, known as the fusion model, is trained using both absolute and relative poses from the training set. During the evaluation stage, the fusion model utilizes the absolute and relative poses predicted from testing images to estimate absolute poses.

5. Evaluation

5.1. Hyperparameter Search for SfM

In the first step, we conduct an extensive hyperparameter search for the SfM parameters described in Table 1 using two datasets: a dataset (train3 and test 6) and a handheld dataset (train 4 and test 7). We select the best hyperparameter combinations for point cloud reconstruction and apply

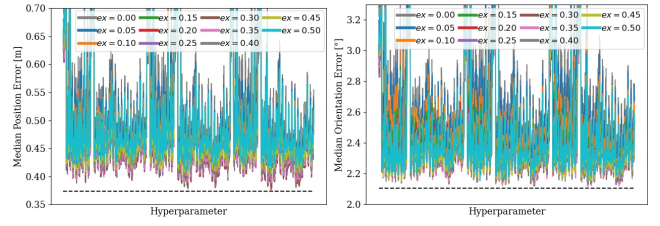

 (a) Median position error in m . (b) Median orientation error in $^\circ$.

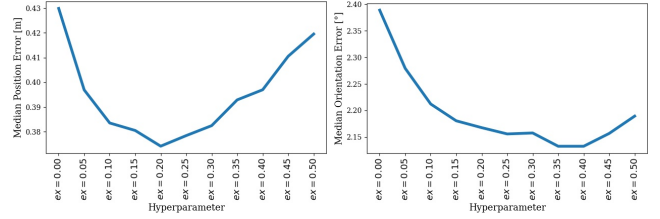
Figure 9: Evaluation of all SfM point clouds (for different hyperparameters, see x-axis) for the handheld train 4 and test 7 datasets. The dashed lines indicate the lowest error.

 (a) Median position error in m . (b) Median orientation error in $^\circ$.

Figure 10: Evaluation of the best SfM point cloud (from Figure 9) for different hyperparameters *exclude* for the handheld train 4 and test 7 datasets.

them to the remaining robotic and handheld datasets. Each dataset (robotic and handheld) comprises a total of 1,752 parameters. Figure 7 illustrates all hyperparameter results for the robot dataset, while we select the best point clouds and evaluate the parameter *exclude* with values in $\{0.0, 0.05, 0.1, 0.15, 0.2, 0.25, 0.3, 0.35, 0.4, 0.45, 0.5, 0.55, 0.6\}$ in Figure 8. We observe that the parameter *exclude* has a significant impact on the position error, with values ranging from $0.24m$ to over $0.7m$. Based on Figure 8, we find that the parameter $ex = 0.30$ yields a low position error of $0.242m$, while the parameter $ex = 0.35$ yields a low orientation error of 1.19° . The hyperparameter search results for the handheld dataset are shown in Figure 9 and Figure 10. The error in this case increases due to the higher dynamics of the human, resulting in a position error of $0.37m$ and orientation error of 2.14° . The optimal value for the parameter *exclude* varies with the position (with $ex = 0.20$ being optimal) and orientation (with $ex = 0.35$ being optimal). To obtain highly accurate orientation predictions, a point cloud with a few and very accurate points is preferred, while a dense point cloud is better for low position error.

Figure 11 and Figure 12 present the selective search for the parameters of the three-point criterion for the robot dataset and the handheld dataset, respectively. We observe that the three-point criterion results in decreased performance (Figures a and c represent the results with the criterion, while Figures b and d show the results without it). Additionally, we explore three other parameters (refer to the legend in Figure c). The first parameter is a hard limit to exclude points, which can be set to either *True* or *False*. We observe an improvement in results when using

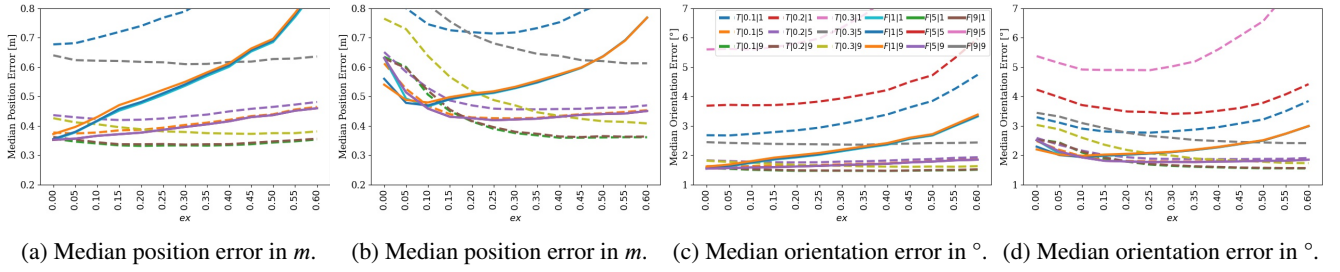


Figure 11: SfM hyperparameter search for the robot train 3 and test 6 datasets. Figures a) and c) are with the three-point criterion, and Figures b) and d) are without the three-point criterion. Legend definition in the corresponding order: With use of the three-point-criterion, i.e., true (T), without use of the three-point criterion, i.e., false (F). If true: $T|oc|sc$. If false: $F|std|sc$. The legend is equal for all subplots.

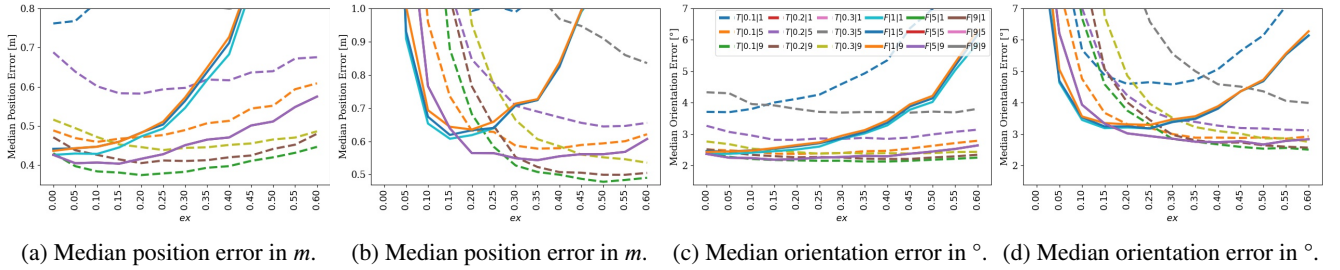


Figure 12: SfM hyperparameter search for the handheld train 4 and test 7 datasets. Figures a) and c) are with the three-point criterion, and Figures b) and d) are without the three-point criterion. Legend definition in the corresponding order: With use of the three-point-criterion, i.e., true (T), without use of the three-point criterion, i.e., false (F). If true: $T|oc|sc$. If false: $F|std|sc$. The legend is equal for all subplots.

the limit. If the limit is used, the second parameter specifies the percentage of lower values to remove from $[0.1, 0.2, 0.3]$, with a preference for lower values. If the limit is set to *False*, we search for the minimum number of neighbors required to not exclude a point, with values in the range $[1, 5, 9]$. The best results are obtained when the number of neighbors is set to 5. The third parameter is the radius, which determines when a point counts as a neighbor for another point, with values in the range $[1, 5, 9]$. Here, a high value is preferred.

The evaluation of additional hyperparameters is presented in Appendix A.1. Figure 27 and Figure 28 show the results for the robot dataset, while Figure 29 and Figure 30 present the results for the handheld dataset. We select the best parameters for fusing with the RPR model.

Table 4

Number of matches per point for the eight training datasets (average and standard deviation).

Dataset	# Matches	Dataset	# Matches
Train 1	9.23 ± 8.41	Train 5	6.86 ± 4.50
Train 2	8.57 ± 6.93	Train 6	7.83 ± 5.73
Train 3	7.72 ± 6.51	Train 7	7.12 ± 4.72
Train 4	7.84 ± 6.29	Train 8	7.89 ± 6.42

5.2. Evaluation Results: SfM

We visualize the resulting SfM point clouds for all training datasets in Figure 13 with the dashed blue lines as the borders of the environment. The open environment

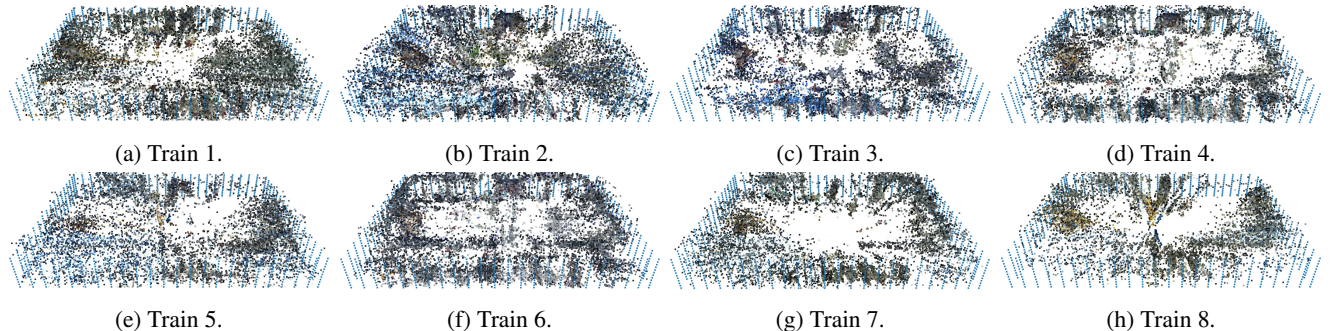


Figure 13: Overview of SfM point clouds for all eight training datasets. Blue dotted lines indicate the borders of the environment.

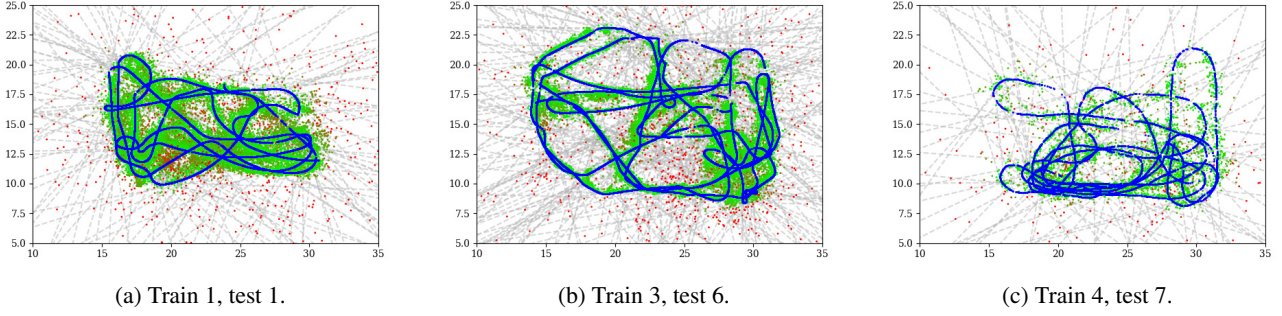


Figure 14: Evaluation of the predicted positions (green $\hat{=}$ low position error, red $\hat{=}$ large position error) against the ground truth trajectories (blue) for SfM.

Table 5

Evaluation results for SfM. Results are shown as median position error in m and median orientation error in $^\circ$. We select the hyperparameter $ex = 0.3$ for the robotic datasets and the hyperparameter $ex = 0.2$ for the handheld datasets. The cell color indicates the relatedness between training and test environments and dynamics (light gray $\hat{=}$ similar environments, dark gray $\hat{=}$ strong environmental differences).

	Train 1		Train 2		Train 3		Train 4		Train 5		Train 6		Train 7		Train 8	
Test 1	0.4406	1.47	0.6720	2.18	0.6820	2.40	1.1758	31.83	1.7932	6.55	0.6600	2.30	2.0009	6.06	6.6378	20.30
Test 2	0.5736	1.94	0.5984	2.14	0.4296	1.71	1.1756	4.02	1.0385	3.64	0.7775	2.69	2.6908	8.47	5.9536	19.22
Test 3	0.8155	2.90	0.7514	2.78	0.4529	1.89	1.7175	6.40	1.5590	5.62	1.1602	3.91	3.4231	11.23	6.5891	21.41
Test 4	1.6407	5.50	0.6393	2.48	0.3407	1.54	1.8450	6.79	1.4746	5.40	1.1674	4.03	7.2445	26.19	7.0458	22.88
Test 5	6.5806	20.27	0.1312	0.82	0.2076	1.05	1.4789	4.79	0.5336	1.85	4.0145	12.14	5.7685	19.70	9.4618	29.55
Test 6	3.8720	13.03	0.7598	2.93	0.2417	1.19	0.5971	2.25	0.5417	1.99	4.3004	13.06	6.7546	23.65	10.3992	35.50
Test 7	24.5902	94.50	15.2681	64.65	1.5336	6.05	0.3742	2.17	0.3458	1.99	21.3927	80.61	18.3089	75.64	20.9043	79.34
Test 8	21.6899	81.23	12.6190	43.84	1.0662	4.41	0.4205	2.22	0.3049	1.82	10.3005	35.54	11.2760	42.33	14.2804	52.24
Test 9	1.0352	3.99	2.0459	6.84	0.8040	3.81	5.9806	18.24	1.0407	4.30	0.5175	2.52	1.5983	5.55	3.8926	12.44
Test 10	1.1925	5.56	5.6020	17.17	1.1586	5.47	2.8885	10.17	1.6000	6.32	0.5515	3.40	0.7954	4.14	4.9886	16.21
Test 11	12.1940	39.80	4.1512	14.22	0.4923	3.27	1.9017	7.29	0.9849	4.58	0.9164	4.34	1.8022	6.10	2.1391	7.25

of the train 1 dataset with no objects allows for a dense reconstruction, while train 2 also yields a high-density point cloud with wall features. However, on the top right and bottom left sections of the hall, points are missing due to the underrepresentation of images in these areas. In contrast, datasets train 3, train 7, and train 8 contain many object features, while train 6 has more ceiling points. Dataset train 4, recorded with slow motions from person 1, has many feature-rich object points, while train 5, with fast motions from person 2, has a higher noise of points due to motion blur. The average number of matches per point cloud, reported in Table 4, supports these findings, with train 1 having the most matches at an average of 9.23 per point, resulting in a dense point cloud. In contrast, train 5 has a lower density with an average of 6.86 matches per point, and the remaining datasets have an average number of matches ranging from 7.12 to 8.57.

Table 5 provides a summary of the SfM results, with the grey cells indicating the difference between the training and testing datasets. The evaluation shows that SfM is highly effective when tested on the same scenario as the training scenario, as evidenced by the low errors on the train 2 and test 5 dataset ($0.1312m$ and 0.82°) and the train 3 and test 6 dataset ($0.2417m$ and 1.19°). For instance, with the point

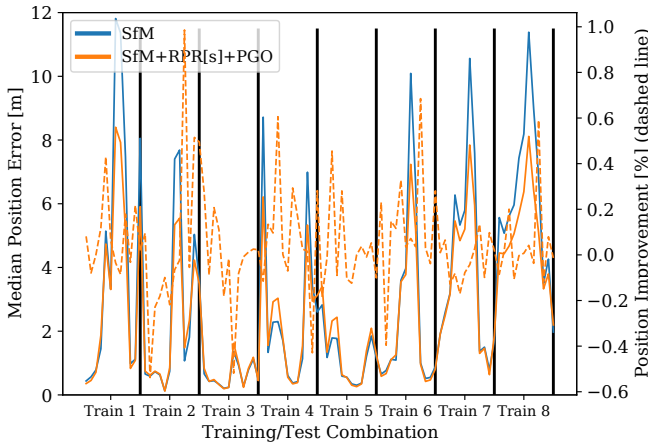
cloud from the train 3 dataset, the error increases consistent with increasing changes in the environment. Therefore, the error correlates with the changes in the environment, i.e., the color of the table cells. On the other hand, the prediction of orientation from the reconstruction is relatively robust against changes, with errors ranging from 1.19° on the test 6 dataset to 2.40° on the test 1 dataset. SfM also performs well on the handheld datasets (train 4 and train 5) with high motion dynamics, when evaluated on the same scenarios (test 7 and test 8). However, SfM fails when the reconstructions are applied to the robot evaluation datasets (and vice versa). In conclusion, while SfM is robust against environmental changes, it is sensitive to dynamics, such as motion blur.

In Figure 14, we present three representative trajectory predictions from SfM. The trajectory predictions for all datasets can be found in Appendix A.2, spanning from Figure 31 to Figure 38. Overall, SfM produces a small number of outliers (specifically, fewer than 100), particularly in scenarios where the test images lack distinctive features. Moreover, SfM can accurately localize the robot in both open environments (see Figure 14a) and those with absorber walls (see Figure 14a). However, the predicted trajectory may not be smooth in some cases (see Figure 14c).

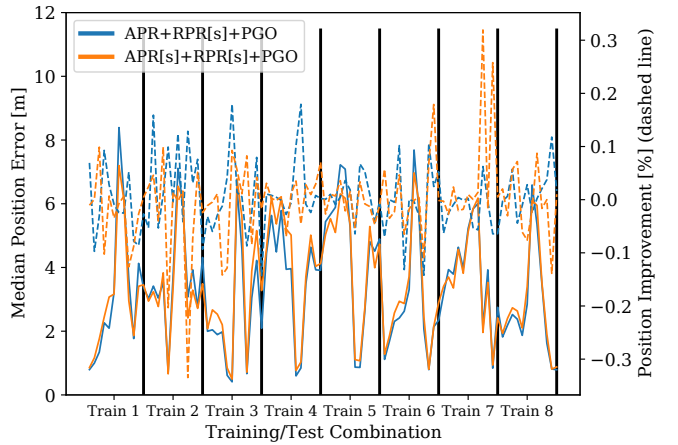
Table 6

Evaluation results for the APR model. Results are shown as median position error in m and median orientation error in $^\circ$. We select the hyperparameter $ex = 0.3$ for the robotic datasets and the hyperparameter $ex = 0.2$ for the handheld datasets. The cell color indicates the relatedness between training and test environments and dynamics (light gray $\hat{=}$ similar environments, dark gray $\hat{=}$ strong environmental differences).

	Train 1		Train 2		Train 3		Train 4		Train 5		Train 6		Train 7		Train 8	
Test 1	0.8076	2.12	3.0364	9.56	2.0245	10.92	4.4608	33.05	5.4224	36.99	1.1224	3.03	3.1848	9.73	1.8310	5.64
Test 2	1.0096	2.98	3.4245	10.36	2.0611	9.47	5.6366	34.33	5.6771	46.69	1.6957	4.83	3.9469	13.93	2.2105	6.09
Test 3	1.3636	4.72	3.0526	12.44	1.9051	9.32	4.5158	35.70	5.9039	42.06	2.3052	8.79	3.8144	18.73	2.5504	8.30
Test 4	2.2635	5.85	3.5413	9.95	1.9869	8.66	5.8072	29.51	7.2380	52.85	2.4261	7.85	4.6354	19.50	2.3831	7.14
Test 5	2.1091	6.93	0.7340	1.99	0.6417	2.32	3.9771	24.13	7.1118	71.50	2.6327	9.32	3.9958	18.60	1.8708	6.64
Test 6	3.2216	23.71	3.7292	19.39	0.4232	1.74	3.9909	16.07	5.2587	43.72	3.3173	30.38	5.2294	54.94	2.8280	23.32
Test 7	8.4233	79.54	7.1442	87.50	6.5239	39.58	0.6277	2.92	0.9070	4.10	7.6766	76.02	5.8731	82.03	6.6052	68.35
Test 8	6.2944	83.48	5.9621	82.11	4.6108	18.77	0.8599	3.88	0.8892	3.85	5.7339	60.65	6.0106	69.61	5.3620	54.91
Test 9	1.7769	5.63	3.9475	18.32	3.0726	21.53	4.6508	34.17	4.8097	41.53	0.8045	2.59	3.9290	8.69	1.6533	4.95
Test 10	4.1898	12.43	2.8045	37.11	4.2577	48.94	3.9608	41.43	4.5296	46.22	2.1423	8.28	0.8444	3.66	0.8224	4.01
Test 11	3.3845	16.54	4.3289	26.20	2.1233	8.81	3.9488	30.08	4.9100	54.42	2.3541	8.53	2.7667	13.89	0.8000	3.82



(a) Fusion of SfM and RPR with PGO.



(b) Fusion of APR and RPR with PGO.

Figure 15: Comparison of SfM, respectively for APR, with the optimization of SfM, respectively of APR, with RPR and PGO. We evaluate APR and RPR pre-trained and non-pre-trained. Dashed lines show the position improvements in %. [s] in APR[s] and RPR[s] defines the pre-trained model with synthetically generated data.

5.3. Evaluation Results: APR and Augmented APR

In this section, an evaluation of the APR model is presented and the results are compared to SfM. The summary of the results is provided in Table 6. Similar to SfM, the APR model achieves the lowest position and orientation errors when evaluated in the same training and testing scenario. However, the errors produced by the APR model are higher compared to SfM (e.g., $0.4232m$ for APR and $0.2417m$ for SfM on the train 3 and test 6 dataset). The error increases significantly when there are variations in the environment (e.g., $2.0245m$ for the test 1 dataset), indicating that the APR model is less robust to changes compared to SfM. On the other hand, the APR model produces fewer outliers due to the restricted area in the learning process.

The motivation behind pre-training the APR model on a synthetically generated dataset is to enhance its generalization capabilities when objects are removed or added. We

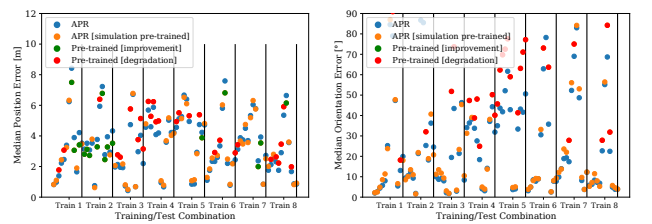

 (a) Median position error in m . (b) Median orientation error in $^\circ$.

Figure 16: Comparison of APR with APR pre-trained on data generated from simulation.

propose a comparison between the results of the APR model and the pre-trained APR model in Figure 16. The x-axis represents all possible combinations of training and testing scenarios. The green dots indicate an improvement in the error, while the red dots indicate a degradation in the error. The simulation environment contains many absorber walls

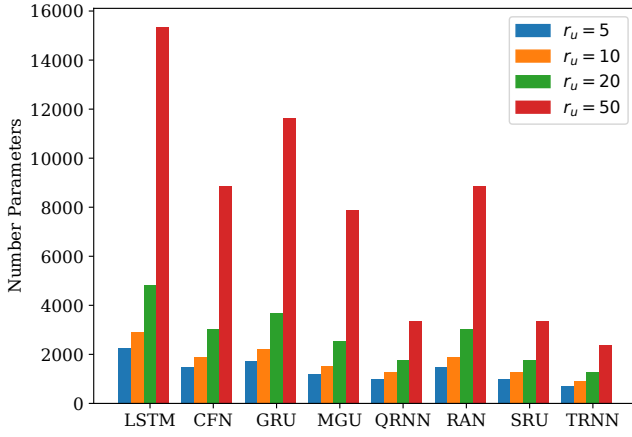


Figure 17: Comparison of trainable model parameters of all eight stacked recurrent networks for APR and RPR fusion for different number of units $r_u \in [5, 10, 20, 50]$.

that resemble the environment of dataset train 2, leading to a significant improvement in results for this scenario. However, the results decrease for the train 4 and train 5 datasets since the synthetic dataset lacks human dynamics and motion blur. When the predicted position error by APR is high, augmenting the data can further improve the results. However, the changes are marginal when the error is already low.

5.4. Fusion Results

In the next step, we conduct an evaluation of the fusion of SfM and RPR, as well as the fusion of APR and RPR. The evaluation initially involves pose refinement using PGO, followed by recurrent fusion cells. For an overview of the evaluation, please refer to Table 3.

PGO & Augmentation. Initially, we refine the absolute poses using relative poses with the state-of-the-art PGO algorithm. Figure 15a presents a comparison between the position error of SfM with the refined poses obtained from PGO (SfM+RPR+PGO). PGO has a significant positive impact on results in challenging scenarios but does not affect good localization results (e.g., train 2, train 3, and train 6 datasets). However, PGO marginally decreases the results for handheld datasets (train 4 and train 5). We also present the percentage improvement achieved when pre-training RPR with simulated data (dashed lines). While pre-training has a negative impact (-0.6%) on the train 2 and train 3 datasets, results can be slightly improved for the remaining datasets, up to 1.0%. Figure 15b presents results for refining APR with RPR. In contrast to SfM, this combination has no effect on results. Additionally, pre-training only leads to marginal improvements or decreases in results.

Recurrent APR-RPR Fusion & Augmentation. In order to fuse APR and RPR and predict an optimized absolute pose, it is essential to consider the specific deterministic, random-walk, non-linear, or long-memory behavior (or a combination of these) of both robotic and human motion.

Specifically, the motion range of objects is limited to certain velocities and orientation changes. To address these challenges, a recurrent unit is necessary to process the required pose information. However, there is currently no clear understanding of which RNN-cell structure is most suitable for each type of behavior and the characterization of these units is not clear (Khaldi et al., 2023). Therefore, we provide a comprehensive evaluation of eight RNN units for the fusion task. According to Khaldi et al. (2023), an MGU cell is most suitable for a deterministic and non-linear behavior, while an LSTM cell is recommended for chaotic behavior, see also Yu et al. (2019). In order to further explore the optimal RNN-cell structure for the fusion task, we train and evaluate in addition to the commonly used cells LSTM, GRU, and MGU, the cell types CFN, QRNN, RAN, SRU, and TRNN. We vary the number of input timestep values ($N_t \in [3, 6, 10, 15, 25]$) and the number of recurrent units ($r_u \in [5, 10, 20, 50]$). Both single and two stacked RNN cells are evaluated using a copy memory task, which is designed to stress test the ability of recurrent networks to propagate long-term, distant information (Bai et al., 2018). This task assesses the model's capacity to retain information for different lengths of time (N_t). To compare the different models, Figure 17 shows the number of trainable model parameters for each of the eight stacked RNN cells and the number of units r_u . We observe that larger cell sizes (r_u) result in a significant increase in trainable parameters, leading to a higher risk of overfitting. On the other hand, smaller gating mechanisms result in a decrease in the number of parameters (i.e., LSTM > GRU > MGU), with TRNN having the fewest parameters. Figure 18 provides an overview of the results for all eight training datasets and various fusions of absolute and relative models (with and without simulated pre-training), compared to PGO (black line). We evaluate the parameters $N_t \in [3, 6, 10, 15, 25]$ and $r_u \in [3, 5, 10]$. We provide rankings for all methods with colored backgrounds. In the following, [s] indicates pre-training. The results of the method ranking indicate that SfM+RPR and SfM+RPR[s] outperform APR on all datasets, except for the train 8 dataset. The efficacy of pre-training is dependent on the dataset. Among the fusion models, most outperform PGO on the train 1, train 2, train 3, train 5, train 6, train 7, and train 8 datasets. Using two stacked RNN cells always yields better results than using only one cell. TRNN (Balduzzi and Ghifary, 2017) consistently achieves the lowest position errors, which is evident in Figures 18a, 18b, 18c, 18d, 18e, and 18f, and 18g. Therefore, a small model with few trainable parameters, i.e., $r_u = 10$ (as shown in Figure 17), is adequate for fusing absolute and relative poses. A large timestep size of $N_t = 25$ is observed to be better, as it enables the model to learn long-term dependencies of the motion dynamics. The difference between the recurrent units $r_u = 5$ and $r_u = 10$ is marginal and varies depending on the dataset, as evident in Figure 18d versus Figure 18h. A model size of $r_u = 3$ is too small to learn usable features.

Table 7 displays the improvement in position compared to SfM-only (Table 5) for all datasets. Depending on the

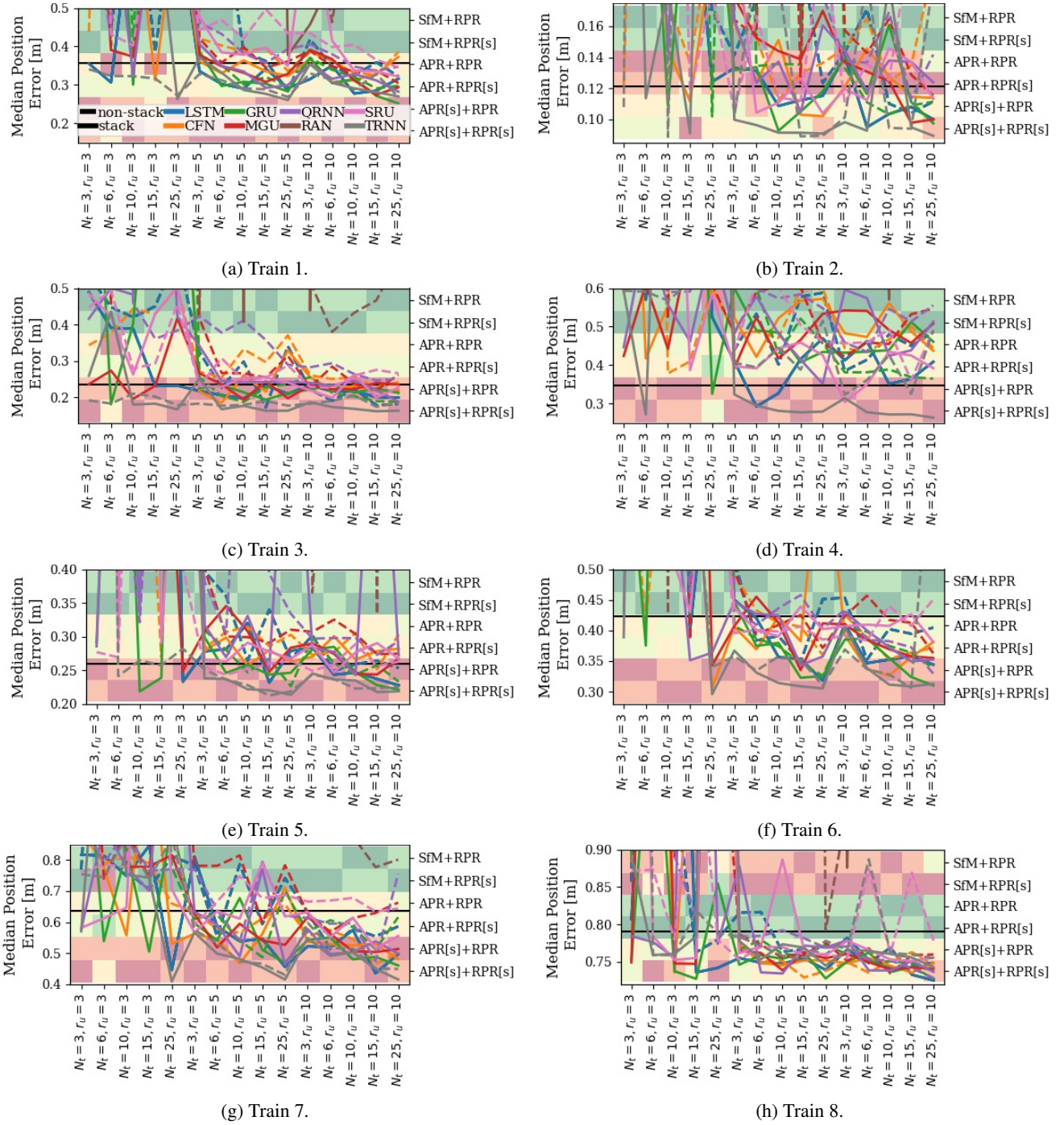


Figure 18: Evaluation of recurrent absolute (i.e., SfM or APR) and relative (i.e., RPR) pose fusion for eight training datasets evaluated on the corresponding testing dataset. Lines evaluate for recurrent cells and stacked (solid) or non-stacked (dashed) cells. The heatmap in the background ranks the best fusion method (green indicates best ranked method and red indicates the last ranked method). [s] indicates the simulation-augmented pre-training of APR or RPR. Black horizontal line indicates the optimization of SfM and RPR with PGO. For readability, we set y limits. The legend is defined in subfigure a) and is consistent.

dataset, the results can demonstrate an improvement ranging from +12.1% to +84.6% for the robotic dataset, especially when the training and testing are conducted on robotic datasets. However, there is a significant decline in results when assessing the handheld dataset on robotic datasets. This suggests that while recurrent cells can learn motion

dynamics and produce a more precise predicted trajectory, they cannot adjust to new dynamics, such as transitioning from fast handheld movements to slow robotic movements. Nevertheless, the model can adapt from robotic to handheld movements. The enhancement is attributed to a significant decrease in outliers and the ability to predict smoothed

Table 7

Evaluation results for the best recurrent cell for fusing SfM or APR with pre-trained RPR utilizing the stacked TRNN cell with N_t timesteps and r_u recurrent units. Results are shown as median position error in m and position improvement in %. The cell color indicates the relatedness between training and test environments and dynamics for the position error (light gray $\hat{=}$ similar environments, dark gray $\hat{=}$ strong environmental differences), and the degree of improvement (green $\hat{=}$ improvement, red $\hat{=}$ degradation) against SfM-only (see Table 5).

	Train 1	Train 2	Train 3	Train 4	Train 5	Train 6	Train 7	Train 8
Test 1	0.2606 +40.9	0.5909 +12.1	0.5249 +23.0	2.5297 -115.1	2.0405 -13.8	0.3877 +41.3	1.4115 +29.5	1.8464 +72.2
Test 2	0.3297 +42.5	0.4970 +16.9	0.3091 +28.0	1.7065 -45.1	1.8001 -73.3	0.4709 +39.4	1.7347 +35.5	2.1859 +63.3
Test 3	0.4724 +42.1	0.5831 +22.4	0.3335 +26.4	1.8748 -9.2	1.9356 -24.2	0.8070 +30.4	1.8795 +45.1	2.5305 +61.6
Test 4	0.9710 +40.8	0.4942 +22.7	0.2394 +29.7	1.8955 -2.7	1.9427 -31.7	0.7822 +33.0	3.5102 +51.5	2.3277 +66.9
Test 5	2.4365 +63.0	0.0888 +32.3	0.1399 +32.6	1.7744 -22.0	1.6923 -217.4	2.2221 +44.6	3.3965 +41.1	1.8474 +80.5
Test 6	1.9714 +49.1	0.6641 +12.6	0.1620 +33.0	1.5941 -184.1	1.6885 -211.7	2.5828 +39.9	3.6296 +46.3	2.7798 +73.3
Test 7	5.7052 +76.8	4.2081 +72.4	1.7238 -12.4	0.2631 +29.7	0.2612 +24.5	5.6267 +73.7	4.6363 +74.7	6.5534 +68.7
Test 8	4.2785 +80.3	4.8111 +61.9	1.8361 -61.7	0.3215 +23.5	0.2125 +30.3	3.5936 +65.1	4.0741 +63.9	5.3554 +62.5
Test 9	0.5803 +43.9	1.4832 +27.5	0.5536 +31.1	2.3406 +60.9	1.7902 -72.0	0.2952 +43.0	1.0633 +33.5	1.6314 +58.1
Test 10	0.6552 +45.1	2.9389 +47.5	0.7821 +32.5	1.9858 +31.3	1.8844 -17.8	0.3701 +32.9	0.4084 +43.7	0.7674 +84.6
Test 11	2.6793 +78.0	2.4830 +40.2	0.3220 +34.6	1.9044 -0.1	1.7822 -81.0	0.5500 +40.0	1.2626 +29.9	0.7451 +65.2

trajectories, which is evident by comparing Figure 20 with Figure 14.

In Figure 19, we present additional results involving 17 convolutional, recurrent, and Transformer models, along with a comparison to PGO and TRNN (as shown in Figure 18). Hyperparameter searches are performed for the following parameters: N_t , r_u , nf , $depth$, d_{model} , and n_{layers} . For the handheld dataset (Figure 19a), only TSiT (Zerveas et al., 2021) and gMLP (Liu et al., 2021) demonstrate superior performance compared to PGO and achieve similar to those of TRNN. However, in the case of the robotic dataset (Figure 19b), most of the methods outperform PGO. Nevertheless, TRNN exhibits lower positioning errors compared to all other methods, except for gMLP.

5.5. Comparison to State-of-the-art

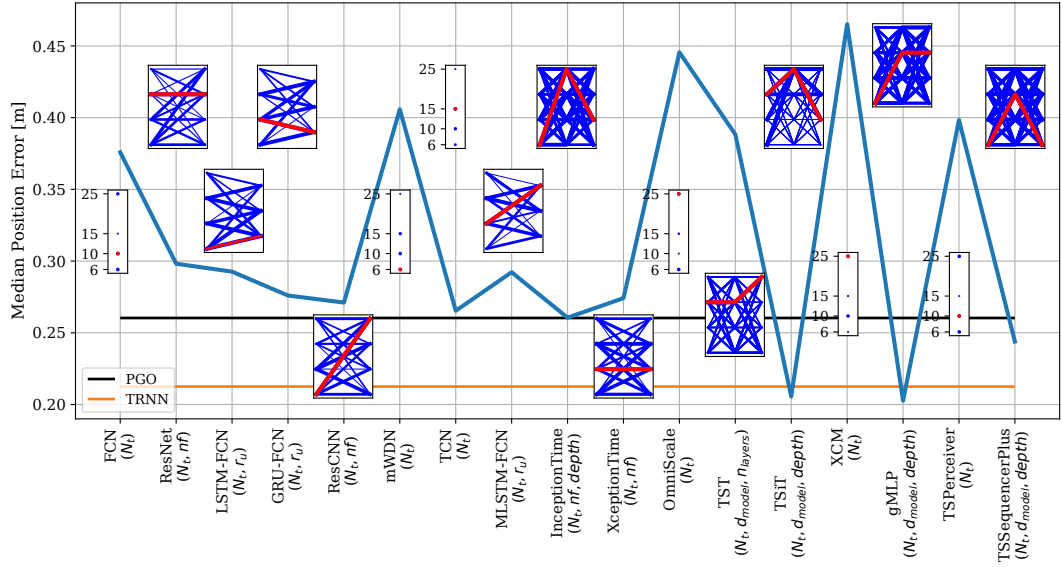
In comparison to state-of-the-art methods, we employ the accelerated coordinate encoding (ACE) technique proposed by Brachmann et al. (2023). ACE leverages a scene-agnostic feature backbone along with a scene-specific prediction head. In their work, Brachmann et al. (2023) utilize an MLP prediction head, enabling optimization across thousands of viewpoints simultaneously during each training iteration. These characteristics leads to a stable and rapid convergence. Notably, ACE represents the most recent advancement in this research domain and has surpassed alternative approaches such as PoseNet (Kendall et al., 2015), MS-Transformer (Shavit et al., 2022), DSAC* (Brachmann and Rother, 2021), SANet (Yang et al., 2019), and SRC (Dong et al., 2022).

Although ACE effectively generates a dense point cloud for nearby objects, such as the large black absorber walls, it struggles to extract features from distant white walls and other feature-rich objects at a distance (see Figure 21). The performance of ACE in pose prediction is notably diminished under challenging conditions, particularly when dealing with absorber walls. In contrast, our point clouds

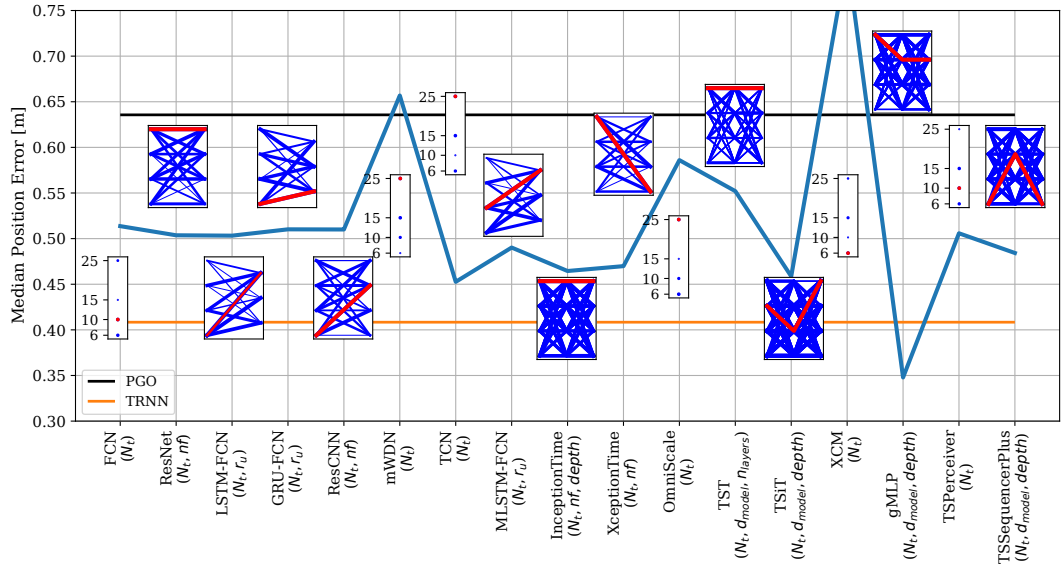
reconstructed with SfM exhibit more evenly distributed features, even from distant walls (see Figure 13). Additionally, we present a comparison of SfM+RPR fusion with TRNN networks and ACE in Table 8. While ACE performs well for scenarios involving close objects, such as in the train 1 and test 3 datasets, our fusion model outperforms ACE in large-scale scenarios, as seen in the train 6 and test 1 dataset. Consequently, for further enhancements in localization results, ACE can be utilized as a black-box model in conjunction with our relative module to achieve a more robust localization solution.

5.6. Robustness to Environmental Challenges

In this section, we aim to investigate the resilience of SfM against environmental variations and challenges. Figure 23 shows the position error for various environmental conditions. Figure 24 illustrates some sample images along with their corresponding matched pixels displayed as red points. One of the primary obstacles is coping with the noise in the input images caused by several factors such as lighting conditions, motion blur, and camera distortion. As depicted in Figure 24b, the presence of motion blur in the image due to the rapid rotation of the robot results in only a few pixels being matched with other images. Conversely, in Figure 24c, a similar background context without motion blur allows for feature extraction from the surroundings, leading to successful matching. The correspondence between the position error in the x (top) and y (bottom) coordinates with respect to the orientation of the camera in the environment, as well as challenges present in the images, is visualized in Figure 22. The x and y-errors exhibit similar behavior. The results indicate that the position error is low for the orientation of 180° , as the feature-rich warehouse racks are visible. However, the position error significantly increases for images that point to the right of the environment (0° and 360°). This is especially evident in the top figure of Figure 22 for the timesteps 200 to 300 and 750 to 1,100, as many absorber walls and reflective surfaces are visible. Selected images recorded



(a) Train 5, test 8.



(b) Train 7, test 10.

Figure 19: Hyperparameter search for the convolutional, recurrent convolutional, and Transformer models. We search for the hyperparameters $N_t \in [5, 10, 15, 25]$, $r_u \in [3, 5, 10]$, $nf \in [16, 32, 64, 128]$, $depth \in [3, 4, 5, 6]$, $d_{model} \in [32, 64, 128, 256]$, and $n_{layers} \in [2, 3, 4, 5]$ (ordered from bottom to top). We select the best hyperparameters (marked red) to compare with PGO (black) and TRNN (orange).

under optimal conditions (green) result in a low position error (e.g., at the timesteps 0 to 150 and 1,250 to 1,350). SfM is found to be robust against slight motion blur, as evident from timestep 2,600 to 2,750. The images in Figure 24d and Figure 24e contain rich information, leading to many pixels being matched. However, SIFT struggles to extract features from the black absorber walls present in Figure 24a and Figure 24e. Additionally, the images were generated using a fish-eye lens in the simulated environment, making it challenging to undistort them to construct an effective point cloud. Moreover, SfM techniques can encounter difficulties when dealing with large-scale scenes. In such scenarios, the number of features and images can become too substantial

for the algorithms to handle efficiently (Schönberger and Frahm, 2016). As a result, we were unable to construct point clouds from more than 1,000 images due to computation times on our hardware setup. Thus, we opted for 600 images for each dataset. One further challenge in SfM is dealing with moving objects in the scene. While our scenarios are static, there are moving objects present between the scenarios. Figure 25 illustrates the average number of matches per image view, which affects the point cloud density. A larger number of matches per view, up to 70 matches (as in Figure 25a), results in a denser point cloud (as in Figure 13a), whereas for the train 8 dataset, the point cloud is sparse (see Figure 13h) due to numerous objects and absorber walls and a smaller

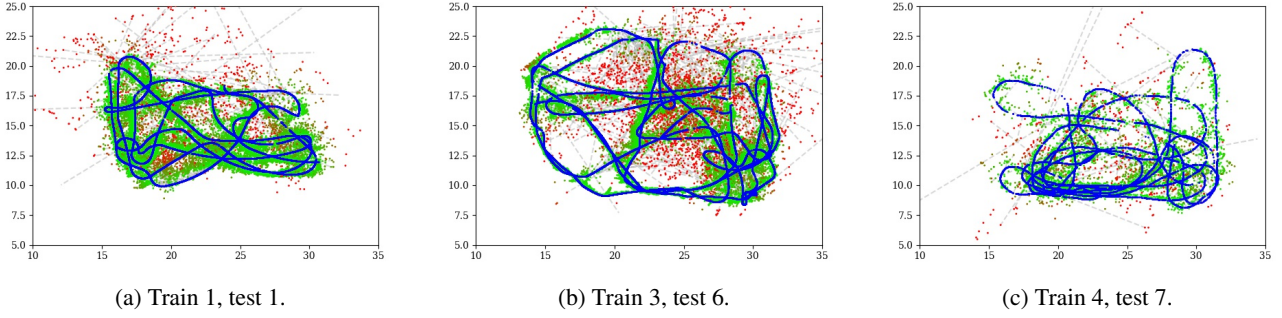


Figure 20: Evaluation of the predicted positions (green $\hat{=}$ low position error, red $\hat{=}$ large position error) against the ground truth trajectories (blue) for the recurrent fusion of SfM with the pre-trained RPR model utilizing the stacked TRNN cell with $N_t = 15$ timesteps and $r_u = 10$ recurrent units.

Table 8

Comparison of results for the TRNN fusion model (left column) with ACE (Brachmann et al., 2023) (right column). Results are shown as median position error in m . The cell color indicates the relatedness between training and test environments and dynamics (light gray $\hat{=}$ similar environments, dark gray $\hat{=}$ strong environmental differences).

	Train 1		Train 2		Train 3		Train 4		Train 5		Train 6		Train 7		Train 8	
Test 1	0.2606	0.271	0.5909	0.329	0.5249	0.492	2.5297	2.522	2.0405	1.701	0.3877	0.484	1.4115	1.619	1.8464	1.939
Test 2	0.3297	0.135	0.4970	0.510	0.3091	0.414	1.7065	1.349	1.8001	1.557	0.4709	0.559	1.7347	1.829	2.1859	2.130
Test 3	0.4724	0.166	0.5831	0.430	0.3335	0.369	1.8748	1.233	1.9356	1.369	0.8070	0.779	1.8795	1.714	2.5305	1.175
Test 4	0.9710	0.263	0.4942	0.495	0.2394	0.273	1.8955	1.044	1.9427	1.267	0.7822	0.755	3.5102	3.687	2.3277	0.958
Test 5	2.4365	2.715	0.0888	0.096	0.1399	0.114	1.7744	0.541	1.6923	0.618	2.2221	2.040	3.3965	3.583	1.8474	1.033
Test 6	1.9714	0.660	0.6641	0.687	0.1620	0.175	1.5941	0.830	1.6885	0.788	2.5828	2.235	3.6296	4.430	2.7798	1.612
Test 7	5.7052	3.550	4.2081	3.588	1.7238	0.418	0.2631	0.216	0.2612	0.227	5.6267	5.325	4.6363	5.317	6.5534	3.998
Test 8	4.2785	2.281	4.8111	1.130	1.8361	0.402	0.3215	0.325	0.2125	0.225	3.5936	3.645	4.0741	4.441	5.3554	2.686
Test 9	0.5803	0.319	1.4832	0.864	0.5536	0.977	2.3406	1.710	1.7902	1.894	0.2952	0.213	1.0633	1.014	1.6314	0.743
Test 10	0.6552	0.423	2.9389	1.198	0.7821	1.233	1.9858	1.561	1.8844	1.733	0.3701	0.535	0.4084	0.365	0.7674	0.431
Test 11	2.6793	2.676	2.4830	1.737	0.3220	0.426	1.9044	0.925	1.7822	1.526	0.5500	0.678	1.2626	1.239	0.7451	0.783

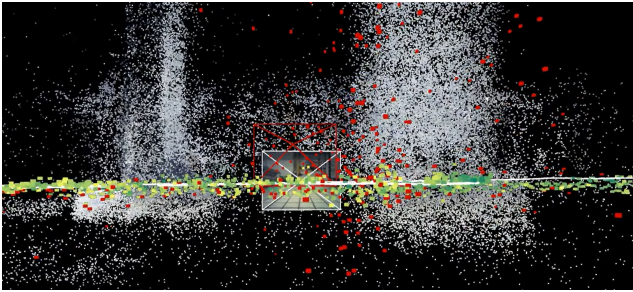


Figure 21: Retrieving absolute poses from the point cloud reconstructed with ACE (Brachmann et al., 2023).

number of matches per view, up to 20, as in Figure 25h. We observe that the number of matches varies significantly across different scenarios, indicating diverse environmental conditions in different areas.

In our analysis of the predicted trajectories (refer to the appendix, Figure 31 to Figure 38), we observed an increase in error in the reconstructed position when constructing a point cloud from a clear environment (train 1) and evaluating it in environments with absorber walls. This trend is noticeable in the top region of test 2, which contains one absorber wall (see Figure 31b), and the lower middle region of test

6, which contains four absorber walls (see Figure 31e). This pattern is also evident in the other datasets we evaluated.

Bundle Adjustment. The verification of BA's effectiveness entails conducting experiments to evaluate its performance in 3D point reconstruction. Therefore, we assessed the performance of BA by varying the hyperparameter std during parameter search. The std parameter primarily influences the performance in handling outlier results. Thus, the selection of an appropriate parameter for BA is crucial, although BA exhibits satisfactory performance within the SfM framework. To further validate our findings, we compared the performance of our utilized SfM method with that of the ACE method, demonstrating that both approaches yield satisfactory reconstructions of 3D point clouds. Additionally, we conducted a reprojection error analysis by computing the reprojection error for each observed feature point before and after applying BA. This error metric quantifies the disparity between the observed feature points in the input images and their corresponding projections onto the reconstructed 3D scene. We observed a substantial reduction in reprojection error following the application of BA, indicating an enhanced alignment between the observed feature points and their respective projections.

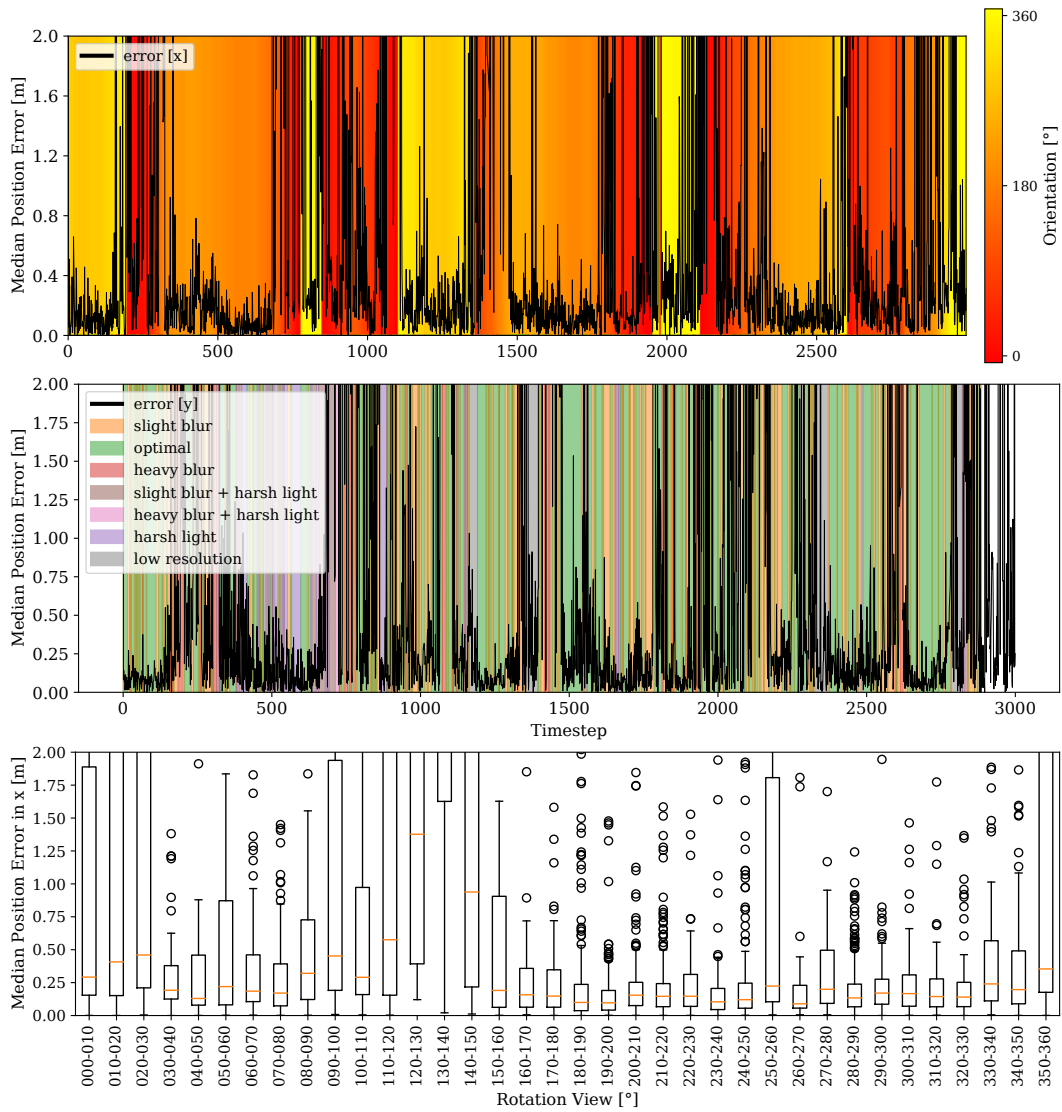


Figure 22: Plot of the positional error with respect to the x and y -coordinates of SfM for the train 4 dataset with environmental challenges marked in color. The top plot shows the orientation between 0° and 360° . The orientation of 0° points to the east of the environment. The middle plot shows seven challenges or optimal image conditions in color. The bottom plot shows the error dependent on the orientation in the environment.

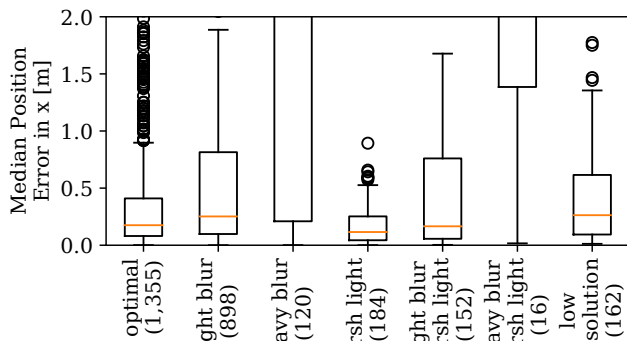


Figure 23: Position error of SfM for various environmental challenges. Number in brackets are the number of samples in the test set.

5.7. Computation Times

Figure 26 depicts the computation times (in s) of Structure from Motion (SfM) for point cloud reconstruction across various parameters: std , mm , sc , oc , ex , and $gibbs$. We highlight each parameter, averaging over the remaining parameters, and present the standard deviation in grey. The time is shown on a logarithmic scale. As observed in Figure 26a, the standard deviation (std) for point exclusion in Bundle Adjustment (BA) minimally affects computation time. The number of minimum matches ($mm \in \{3, 4, 5\}$) impacts the time for cluster separation, as demonstrated in Figure 26b. Higher spatial consistency (sc) results in increased time for match computation and view correction, as depicted in Figure 26c, due to the utilization of k-means. The overlap criterion (oc) in Figure 26d and separation limits (ex) in Figure 26e have a marginal impact on training

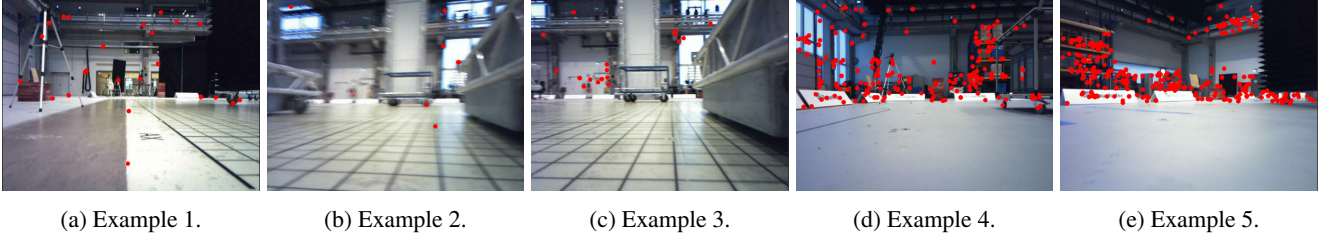


Figure 24: Matches in red for five exemplary images.

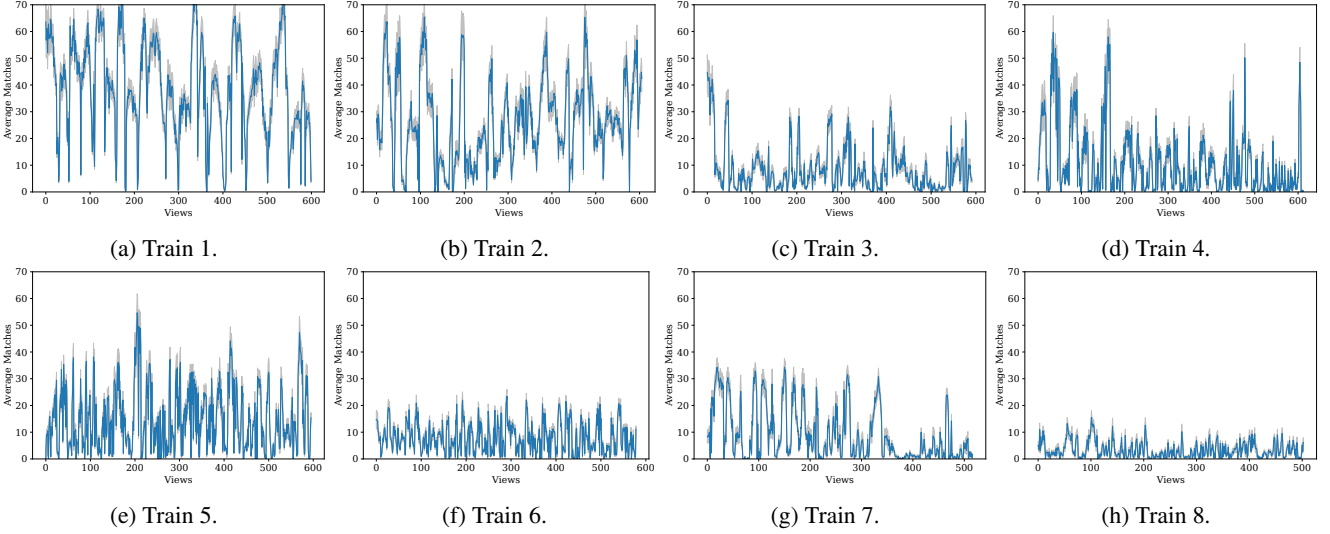


Figure 25: Average number of matches (y-axis) per view (x-axis) for all eight training datasets. Grey indicates standard deviation over all images.

time. Generally, cluster separation and 3D pose estimation from BA are the most time-consuming steps. SfM offers the advantage of being executable on a small CPU.

6. Conclusion

The application field of the proposed method extends beyond real-time self-localization of objects, such as robots and humans, within small-scale and large-scale environments. It also encompasses various other fields such as autonomous vehicles, where precise localization is crucial for navigation and obstacle avoidance. Additionally, the method can be applied in augmented reality and virtual reality systems, enabling accurate tracking of users' movements and interactions with virtual objects. Furthermore, in the context of smart cities, the method can support location-based services, urban planning, and traffic management by providing real-time localization of vehicles, pedestrians, and infrastructure elements.

The primary focus of our study was to integrate absolute poses obtained from structure from motion (SfM) or an absolute pose regression (APR) method with relative poses, aiming to optimize and smooth the trajectory of objects such as robots and humans. For estimating the relative pose, we introduced a recurrent network that learns translation and rotation by analyzing optical flow between consecutive

images computed using the Lucas-Kanade algorithm. Our key contribution was a fusion framework employing eight different recurrent neural networks to combine absolute and relative poses. We compared our approach to the state-of-the-art pose graph optimization (PGO) technique for pose refinement. Additionally, we introduced a large visual database recorded in a challenging indoor environment resembling warehouse scenarios. Furthermore, we developed a simulation framework for generating synthetic images to pre-train APR and RPR models, facilitating faster training.

After conducting a thorough evaluation on the datasets, we have identified several key findings: (1) The quality of the point cloud generated by structure from motion (SfM) is heavily influenced by the chosen hyperparameters, particularly those related to point removal, impacting both position and orientation errors significantly. (2) Careful parameter selection leads to notably better outcomes compared to pose regression techniques. (3) Both SfM and absolute pose regression (APR) methods encounter challenges in extracting features from difficult images, particularly those lacking distinctive features. However, APR methods demonstrate greater resilience to environmental changes. (4) Pre-training APR and relative pose regression (RPR) models results in a slight improvement in position error, up to 1%, particularly in environments resembling the simulated scenario. (5) Pose graph optimization (PGO) effectively refines poses, reducing

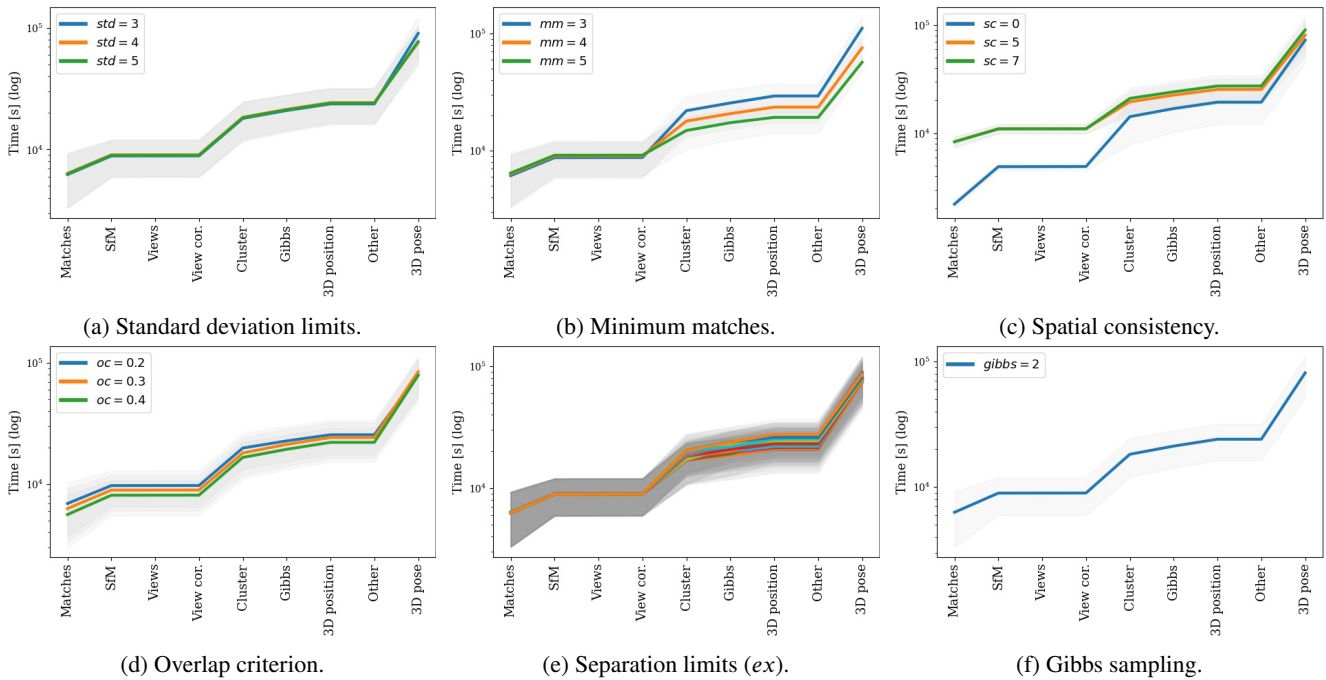


Figure 26: Overview of computation times (logarithmic in s) for different hyperparameter choices.

high position errors while also minimizing low position errors. (6) Our framework, incorporating various fusion cells based on convolutional, recurrent, and Transformer models, significantly enhances absolute pose error, enabling smoother trajectories and greater resilience to challenges. This approach consistently surpasses PGO. Implementing a strongly-typed Recurrent Neural Network (TRNN) as a small-scale RNN model has led to an average improvement of 42.67% in position results over SfM-only results for the robotic datasets.

Acknowledgments

This work was supported by the Federal Ministry of Education and Research (BMBF) of Germany by Grant No. 01IS18036A (David Rügamer), as well as by the Bavarian Ministry for Economic Affairs, Infrastructure, Transport and Technology through the Center for Analytics-Data-Applications (ADA-Center) within the framework of “BAY-ERN DIGITAL II”.

Declaration of competing interest

The authors declare that they have no known competing financial interests or personal relationships that could have appeared to influence the work reported in this paper.

Data statement

For reproducibility and transparency, we publish our datasets and software on the following website: https://gitlab.cc-asp.fraunhofer.de/ottf/industry_datasets. The repository includes the eight training and 11 testing datasets,

the selected images for structure from motion, the checkerboard images for calibration, the synthetically generated dataset, the point clouds recorded with the NavVis M4 system, and all ground truth poses. Additionally, we publish the source code. The repository is 798 GB in size in total.

CRediT authorship contribution statement

Felix Ott: conceptualization of this study, methodology, software, validation, formal analysis, investigation, data curation, writing – original draft, writing – review & editing, visualization, data recording, project administration. **Lucas Heublein:** conceptualization of this study, methodology, software, investigation, data curation. **David Rügamer:** formal analysis, writing – review & editing, visualization, supervision. **Bernd Bischl:** supervision. **Christopher Mutschler:** resources, writing – review & editing, supervision, funding acquisition.

References

- Acharya, D., Tatli, C.J., Khoshelham, K., 2023. Synthetic-Real Image Domain Adaptation for Indoor Camera Pose Regression Using a 3D Model, in: ISPRS Journal of Photogrammetry and Remote Sensing (P&RS), pp. 405–421. doi:10.1016/j.isprsjprs.2023.06.013.
- Bai, S., Kolter, J.Z., Koltun, V., 2018. An Empirical Evaluation of Generic Convolutional and Recurrent Networks for Sequence Modeling, in: arXiv preprint arXiv:1803.01271v1 [cs.LG]. doi:10.48550/arXiv.1803.01271.
- Baker, S., Matthews, I., 2004. Lucas-Kanade 20 Years on: A Unifying Framework, in: Intl. Journal of Computer Vision (IJCV), pp. 221–255. doi:10.1023/B:VISI.0000011205.11775.fd.
- Balduzzi, D., Ghifary, M., 2017. Strongly-Typed Recurrent Neural Networks, in: Proc. of the Intl. Conf. on Machine Learning (ICML), New York, NY. pp. 1292–1300.

- Barros, A.M., Michel, M., Moline, Y., Corre, G., Carrel, F., 2022. A Comprehensive Survey of Visual SLAM Algorithms, in: MDPI Robotics. doi:10.3390/robotics11010024.
- Bay, H., Tuytelaars, T., Gool, L.V., 2006. SURF: Speeded Up Robust Features, in: Europ. Conf. on Computer Vision (ECCV), pp. 404–417. doi:10.1007/11744023_32.
- Blanton, H., 2021. Revisiting Absolute Pose Regression, in: Dissertations, University of Kentucky.
- Boittiaux, C., Marxer, R., Dune, C., Arnaubec, A., Hugel, V., 2022. Homography-Based Loss Function for Camera Pose Regression, in: IEEE Robotics and Automation Letters (RA-L), pp. 6242–6249. doi:10.1109/LRA.2022.3168329.
- Brachmann, E., Cavallari, T., Prisacariu, V.A., 2023. Accelerated Coordinate Encoding: Learning to Relocalize in Minutes Using RGB and Poses, in: Proc. of the IEEE/CVF Intl. Conf. on Computer Vision and Pattern Recognition (CVPR).
- Brachmann, E., Rother, C., 2021. Visual Camera Relocalization from RGB and RGB-D Images Using DSAC, in: IEEE Trans. on Pattern Analysis and Machine Intelligence (TPAMI), pp. 5847–5865. doi:10.1109/TPAMI.2021.3070754.
- Bradbury, J., Merity, S., Xiong, C., Socher, R., 2017. Quasi-Recurrent Neural Networks, in: Intl. Conf. on Learning Representations (ICLR), Toulon, France.
- Brahmbhatt, S., Gu, J., Kim, K., Hays, J., Kautz, J., 2018. Geometry-Aware Learning of Maps for Camera Localization, in: Proc. of the IEEE/CVF Intl. Conf. on Computer Vision and Pattern Recognition (CVPR), Salt Lake City, UT, pp. 2616–2625. doi:10.1109/CVPR.2018.00277.
- Brieger, T., Raichur, N.L., Jdidi, D., Ott, F., Feigl, T., van der Merwe, J.R., Rügamer, A., Felber, W., 2022. Multimodal Learning for Reliable Interference Classification in GNSS Signals, in: Proc. of the Intl. Technical Meeting of the Satellite Division of the Institute of Navigation (ION GNSS+), Denver, CO, pp. 3210–3234. doi:10.33012/2022.18586.
- Chidlovskii, B., Sadek, A., 2021. Adversarial Transfer of Pose Estimation Regression, in: Europ. Conf. on Computer Vision Workshops (ECCVW). doi:10.1007/978-3-030-66415-2_43.
- Chung, J., Gulcehre, C., Cho, K., Bengio, Y., 2014. Empirical Evaluation of Gated Recurrent Neural Networks on Sequence Modeling, in: arXiv preprint arXiv:1412.3555.v1 [cs.NE]. doi:10.48550/arXiv.1412.3555.
- Clark, R., Wang, S., Wen, H., Markham, A., Trigoni, N., 2017. ViNet: Visual-Inertial Odometry as a Sequence-to-Sequence Learning Problem, in: Proc. of the AAAI Conf. on Artificial Intelligence (AAAI), pp. 3995–4001. doi:10.5555/3298023.3298149.
- Costante, G., Ciarfuglia, T.A., 2018. LS-VO: Learning Dense Optical Subspace for Robust Visual Odometry Estimation, in: IEEE Robotics and Automation Letters (RA-L), pp. 1735–1742. doi:10.1109/LRA.2018.2803211.
- Das, A., Dubbelman, G., 2018. An Experimental Study on Relative and Absolute Pose Graph Fusion for Vehicle Localization, in: IEEE Intelligent Vehicles Symposium (IV), Changshu, Suzhou, China, pp. 630–635.
- Ding, X., Wang, Y., Tang, L., Jiao, Y., Xiong, R., 2020. Improving the Generalization of Network Based Relative Pose Regression: Dimension Reduction as a Regularizer, in: arXiv preprint arXiv:2010.12796.v1 [cs.CV]. doi:10.48550/arXiv.2010.12796.
- Dong, S., Wang, S., Zhuang, Y., Kannala, J., Pollefeys, M., Chen, B., 2022. Visual Localization via Few-shot Scene Region Classification, in: IEEE Intl. Conf. on 3D Vision (3DV), Prague, Czech Republic. doi:10.1109/3DV57658.2022.00051.
- Dosovitskiy, A., Fischer, P., Ilg, E., Häusser, P., Hazirbas, C., Golkov, V., van der Smagt, P., Cremers, D., Brox, T., 2015. FlowNet: Learning Optical Flow with Convolutional Networks, in: Proc. of the IEEE/CVF Intl. Conf. on Computer Vision (ICCV), Santiago de Chile, Chile, pp. 2758–2766. doi:10.1109/ICCV.2015.316.
- Elsayed, N., Maida, A.S., Bayoumi, M., 2019. Deep Gated Recurrent and Convolutional Network Hybrid Model for Univariate Time Series Classification, in: Intl. Journal of Advanced Computer Science and Applications (IJACSA). doi:10.14569/IJACSA.2019.0100582.
- Emter, T., Schirg, A., Woock, P., Peterleit, J., 2019. Stochastic Cloning for Robust Fusion of Multiple Relative and Absolute Measurements, in: IEEE Intelligent Vehicles Symposium (IV), Paris, France.
- Fauvel, K., Élisabeth Fromont, Masson, V., Faverdin, P., Termier, A., 2022. XEM: An Explainable-by-Design Ensemble Method for Multivariate Time Series Classification, in: WIREs Data Mining and Knowledge Discovery, pp. 917–957. doi:10.1007/s10618-022-00823-6.
- Fawaz, H.I., Lucas, B., Forestier, G., Pelletier, C., Schmidt, D.F., Weberf, J., Webb, G.I., Idoumghar, L., Muller, P.A., Petitjean, F., 2020. InceptionTime: Finding AlexNet for Time Series Classification, in: WIREs Data Mining and Knowledge Discovery, pp. 1936–1962. doi:10.1007/s10618-020-00710-y.
- Fuentes-Pacheco, J., Ruiz-Ascencio, J., Rendón-Mancha, J.M., 2012. Visual Simultaneous Localization and Mapping: A Survey, in: Artificial Intelligence Review, pp. 55–81. doi:10.1007/s10462-012-9365-8.
- GitHub (jahdiel), 2016. pySBA – Python Bundle Adjustment, in: Github: <https://github.com/jahdiel/pySBA>.
- Godard, C., Aodha, O.M., Firman, M., Brostow, G.J., 2019. Digging Into Self-Supervised Monocular Depth Estimation, in: Proc. of the IEEE/CVF Intl. Conf. on Computer Vision (ICCV), pp. 3828–3838.
- Graves, A., Liwicki, M., Fernández, S., Bertolami, R., Bunke, H., Schmidhuber, J., 2009. A Novel Connectionist System for Unconstrained Handwriting Recognition, in: IEEE Trans. on Pattern Analysis and Machine Intelligence (TPAMI), pp. 855–868. doi:10.1109/TPAMI.2008.137.
- Han, L., Lin, Y., Du, G., Lian, S., 2019. DeepVIO: Self-supervised Deep Learning of Monocular Visual Inertial Odometry using 3D Geometric Constraints, in: IEEE/RSJ Intl. Conf. on Intelligent Robots and Systems (IROS), Macau, China. doi:10.1109/IROS40897.2019.8968467.
- Heck, J.C., Salem, F.M., 2017. Simplified Minimal Gated Unit Variations for Recurrent Neural Networks, in: IEEE Intl. Midwest Symposium on Circuits and Systems (MWSCAS), Boston, MA. doi:10.1109/MWSCAS.2017.8053242.
- Hochreiter, S., Schmidhuber, J., 1997. Long Short-Term Memory, in: Neural Computation, pp. 1735–1780.
- Huang, A.S., Bachrach, A., Henry, P., Kraining, M., Maturana, D., Fox, D., Rox, N., 2011. Visual Odometry and Mapping for Autonomous Flight Using an RGB-D Camera, in: ISRR.
- Idan, O., Shavit, Y., Keller, Y., 2023. Learning to Localize in Unseen Scenes with Relative Pose Regressors, in: arXiv preprint arXiv:2303.02717v1 [cs.CV]. doi:10.48550/arXiv.2303.02717.
- Ilg, E., Mayer, N., Saikia, T., Keuper, M., Dosovitskiy, A., Brox, T., 2017. FlowNet 2.0: Evolution of Optical Flow Estimation with Deep Networks, in: Proc. of the IEEE/CVF Intl. Conf. on Computer Vision and Pattern Recognition (CVPR), Honolulu, HI, pp. 1647–1655. doi:10.1109/CVPR.2017.179.
- Iyer, G., Murthy, J.K., Gupta, G., Krishna, K.M., Paull, L., 2018. Geometric Consistency for Self-Supervised End-to-End Visual Odometry, in: Proc. of the IEEE/CVF Computer Vision and Pattern Recognition Workshops (CVPRW), Salt Lake City, UT. doi:10.1109/CVPRW.2018.00064.
- Jaegle, A., Borgeaud, S., Alayrac, J.B., Doersch, C., Ionescu, C., Ding, D., Koppula, S., Zoran, D., Brock, A., Shelhamer, E., Hénaff, O., Botvinick, M.M., Zisserman, A., Vinyals, O., ao Carreira, J., 2021. Perceiver IO: A General Architecture for Structured Inputs & Outputs, in: Intl. Conf. on Learning Representations (ICLR).
- Jiang, S., Jiang, C., Jiang, W., 2020. Efficient Structure from Motion for Large-scale UAV images: A Review and a Comparison of SfM Tools, in: ISPRS Journal of Photogrammetry and Remote Sensing (P&RS), pp. 230–251. doi:10.1016/j.isprsjprs.2020.04.016.
- Karim, F., Majumdar, S., Darabi, H., Chen, S., 2017. LSTM Fully Convolutional Networks for Time Series Classification, in: IEEE Access, pp. 1662–1669. doi:10.1109/ACCESS.2017.2779939.
- Karim, F., Majumdar, S., Darabi, H., Harford, S., 2019. Multivariate LSTM-FCNs for Time Series Classification, in: Neural Network, pp. 237–245. doi:10.1016/j.neunet.2019.04.014.
- Kazerouni, I.A., Fitzgerald, L., Dooly, G., Toal, D., 2022. A Survey of State-of-the-art on Visual SLAM, in: Expert Systems with Applications. doi:10.1016/j.eswa.2022.117734.

- Kendall, A., Grimes, M., Cipolla, R., 2015. PoseNet: A Convolutional Network for Real-Time 6-DOF Camera Relocalization, in: Proc. of the IEEE/CVF Intl. Conf. on Computer Vision (ICCV), Santiago de Chile, Chile. pp. 2938–2946. doi:10.1109/ICCV.2015.336.
- Khalidi, R., Afia, A.E., Chiheb, R., Tabik, S., 2023. What is the Best RNN-cell Structure to Forecast Each Time Series Behavior, in: Expert Systems with Applications. doi:10.1016/j.eswa.2022.119140.
- Kim, D., Kim, J., 2023. CT-Loc: Cross-domain Visual Localization with a Channel-wise Transformer, in: Neural Networks, pp. 369–383. doi:10.1016/j.neunet.2022.11.014.
- Kreuzig, R., Ochs, M., Mester, R., 2019. DistanceNet: Estimating Traveled Distance From Monocular Images Using a Recurrent Convolutional Neural Network, in: Proc. of the IEEE/CVF Computer Vision and Pattern Recognition Workshops (CVPRW), Long Beach, CA. doi:10.1109/CVPRW.2019.00165.
- Laurent, T., von Brecht, J., 2017. A Recurrent Neural Network Without Chaos, in: Intl. Conf. on Learning Representations (ICLR), Toulon, France.
- Lee, K., Levy, O., Zettlemoyer, L., 2017. Recurrent Additive Networks, in: arXiv preprint arXiv:1705.07393.v2 [cs.CL]. doi:10.48550/arXiv.1705.07393.
- Lei, T., Zhang, Y., Artzi, Y., 2017. Training RNNs as Fast as CNNs, in: arXiv preprint arXiv:1709.02755v3 [cs.CL]. doi:10.48550/arXiv.1709.02755.
- Li, J., Zhao, J., Song, S., Feng, T., 2021. Unsupervised Joint Learning of Depth, Optical Flow, Ego-motion from Video, in: arXiv preprint arXiv:2105.14520.
- Li, Q., Cao, R., Zhu, J., Fu, H., Zhou, B., Fang, X., Jia, S., Zhang, S., Liu, K., Li, Q., 2023a. Learn Then Match: A Fast Coarse-to-fine Depth Image-based Indoor Localization Framework for Dark Environments via Deep Learning and Keypoint-based Geometry Alignment, in: ISPRS Journal of Photogrammetry and Remote Sensing (P&RS), pp. 169–177. doi:10.1016/j.isprsjprs.2022.10.015.
- Li, X., Ling, H., 2022. GTCaR: Graph Transformer for Camera Relocalization, in: Europ. Conf. on Computer Vision (ECCV), pp. 229–246. doi:10.1007/978-3-031-20080-9_14.
- Li, Y., Cao, R., Liu, K., Li, Z., Zhu, J., Bao, Z., Fang, X., Li, Q., Huang, X., Qiu, G., 2023b. Structure-Guided Camera Localization for Indoor Environments, in: ISPRS Journal of Photogrammetry and Remote Sensing (P&RS), pp. 219–229. doi:10.1016/j.isprsjprs.2023.05.034.
- Lin, Y., Liu, Z., Huang, J., Wang, C., Du, G., Bai, J., Lian, S., Huang, B., 2019. Deep Global-Relative Networks for End-to-End 6-DoF Visual Localization and Odometry, in: Proc. of the Pacific Rim Intl. Conf. Artificial Intelligence (PRICAI), Cuvu, Fiji. pp. 454–467. doi:10.1007/978-3-030-29911-8_35.
- Liu, H., Dai, Z., So, D.R., Le, Q.V., 2021. Pay Attention to MLPs, in: Advances in Neural Information Processing Systems (NIPS).
- Löffler, C., Riechel, S., Fischer, J., Mutschler, C., 2018. Evaluation Criteria for Inside-Out Indoor Positioning Systems Based on Machine Learning, in: IEEE Intl. Conf. on Indoor Positioning and Indoor Navigation (IPIN), Nantes, France. pp. 1–8. doi:10.1109/IPIN.2018.8533862.
- Lowe, D.G., 2004. Distinctive Image Features from Scale-Invariant Keypoints, in: Intl. Journal of Computer Vision (IJCV).
- Lu, Y., Lu, G., 2019. Deep Unsupervised Learning for Simultaneous Visual Odometry and Depth Estimation, in: IEEE Intl. Conf. on Image Processing (ICIP), Taipei, Taiwan. doi:10.1109/ICIP.2019.8803247.
- Mansur, S., Habib, M., Pratama, G.N.P., Cahyadi, A.I., Ardiyanto, I., 2017. Real Time Monocular Visual Odometry using Optical Flow: Study on Navigation of Quadrotor's UAV, in: Intl. Conf. on Science and Technology - Computer (ICST), Yogyakarta, Indonesia. pp. 122–126. doi:10.1109/ICSTC.2017.8011864.
- Mirowski, M., Grimes, M.K., Malinowski, M., Hermann, K.M., Anderson, K., Teplyashin, D., Simonyan, K., Kavukcuoglu, K., Zisserman, A., Hadsell, R., 2018. Learning to Navigate in Cities Without a Map, in: Advances in Neural Information Processing Systems (NIPS), pp. 2424–2435.
- Mitsuki, Y., Ryogo, Y., Kanji, T., 2021. S3G-ARM: Highly Compressive Visual Self-Localization from Sequential Semantic Scene Graph Using Absolute and Relative Measurements, in: arXiv preprint arXiv:2109.04569.v2 [cs.CV]. doi:10.48550/arXiv.2109.04569.
- do Monte Lima, J.P.S., Uchiyama, H., ichiro Taniguchi, R., 2019. End-to-End Learning Framework for IMU-based 6-DOF Odometry, in: MDPI Sensors, p. 3777. doi:10.3390/s19173777.
- Muller, B.R., Smith, W.A.P., 2023. Self-supervised Relative Pose with Homography Model-fitting in the Loop, in: Proc. of the IEEE/CVF Winter Conf. for Applications on Computer Vision (WACV), Waikoloa, HI. doi:10.1109/WACV56688.2023.00566.
- Muller, P., Savakis, A., 2017. Flowdometry: An Optical Flow and Deep Learning Based Approach to Visual Odometry, in: Proc. of the IEEE/CVF Winter Conf. for Applications on Computer Vision (WACV), Santa Rosa, CA. pp. 624–631. doi:10.1109/WACV.2017.75.
- Muller, P.M., Savakis, A., Ptucha, R., Melton, R., 2016. Optical Flow and Deep Learning Based Approach to Visual Odometry, in: Thesis, Rochester Institute of Technology, Department of Computer Engineering, Rochester, NY.
- OpenCV, 2022. Introduction to SIFT (Scale-Invariant Feature Transform), in: OpenCV: https://docs.opencv.org/4.x/da/df5/tutorial_py_sift_intro.html.
- Ott, F., Feigl, T., Löffler, C., Mutschler, C., 2020. ViPR: Visual-Odometry-aided Pose Regression for 6DoF Camera Localization, in: Proc. of the IEEE/CVF Computer Vision and Pattern Recognition Workshops (CVPRW), Seattle, WA. pp. 187–198. doi:10.1109/CVPRW50498.2020.00029.
- Ott, F., Raichur, N.L., Rügamer, D., Feigl, T., Neumann, H., Bischl, B., Mutschler, C., 2022a. Benchmarking Visual-Inertial Deep Multimodal Fusion for Relative Pose Regression and Odometry-aided Absolute Pose Regression, in: arXiv preprint arXiv:2208.00919. doi:10.48550/arXiv.2208.00919.
- Ott, F., Rügamer, D., Heublein, L., Bischl, B., Mutschler, C., 2022b. Joint Classification and Trajectory Regression of Online Handwriting using a Multi-Task Learning Approach, in: Proc. of the IEEE/CVF Winter Conf. for Applications on Computer Vision (WACV), Waikoloa, HI. pp. 266–276. doi:10.1109/WACV51458.2022.00131.
- Parameshwara, C.M., Hari, G., Fermüller, C., Sanket, N.J., Aloimonos, Y., 2022. DiffPoseNet: Direct Differentiable Camera Pose Estimation, in: Proc. of the IEEE/CVF Intl. Conf. on Computer Vision and Pattern Recognition (CVPR), New Orleans, LA. doi:10.1109/CVPR52688.2022.00672.
- Pepe, A., Lasenby, J., 2023. CGA-PoseNet: Camera Pose Regression via a 1D-Up Approach to Conformal Geometric Algebra, in: arXiv preprint arXiv:2302.05211v1 [cs.CV].
- Piasco, N., Sidibé, D., Demonceaux, C., Gouet-Brunet, V., 2018. A Survey on Visual-based Localization: On the Benefit of Heterogeneous Data, in: Pattern Recognition, pp. 90–109. doi:10.1016/j.patcog.2017.09.013.
- Qiao, C., Xiang, Z., Fan, Y., Bai, T., Zhao, X., Fu, J., 2023. TransAPR: Absolute Camera Pose Regression with Spatial and Temporal Attention, in: IEEE Robotics and Automation Letters (RA-L), pp. 4633–4640. doi:10.1109/LRA.2023.3286123.
- Radanovic, M., Khoshelham, K., Fraser, C., 2023. Aligning the Real and the Virtual World: Mixed Reality Localisation Using Learning-based 3D-3D Model Registration, in: Advanced Engineering Informatics. doi:10.1016/j.aei.2023.101960.
- Radwan, N., Valada, A., Burgard, W., 2018. VLocNet++: Deep Multitask Learning for Semantic Visual Localization and Odometry, in: IEEE Robotics and Automation Letters (RA-L), pp. 4407–4414. doi:10.1109/LRA.2018.2869640.
- Rahimian, E., Zabihi, S., Atashzar, S.F., Asif, A., Mohammadi, A., 2019. XceptionTime: A Novel Deep Architecture based on Depthwise Separable Convolutions for Hand Gesture Classification, in: arXiv preprint arXiv:1911.03803v1 [cs.LG].
- Resch, B., Lensch, H.P.A., Wang, O., Pollefeys, M., Sorkine-Hornung, A., 2015. Scalable Structure from Motion for Densely Sampled Videos, in: Proc. of the IEEE/CVF Intl. Conf. on Computer Vision and Pattern Recognition (CVPR), Boston, MA. pp. 3936–3944. doi:10.1109/CVPR.2015.7299019.

- Ruan, J., He, L., Guan, Y., Zhang, H., 2023. Combining Scene Coordinate Regression and Absolute Pose Regression for Visual Relocalization, in: IEEE Intl. Conf. on Robotics and Automation (ICRA), London, UK. doi:10.1109/ICRA48891.2023.10160317.
- Rublee, E., Rabaud, V., Konolige, K., Bradski, G., 2011. ORB: An Efficient Alternative to SIFT or SURF, in: Proc. of the IEEE/CVF Intl. Conf. on Computer Vision (ICCV), Barcelona, Spain. doi:10.1109/ICCV.2011.6126544.
- Sattler, T., Zhou, Q., Pollefeys, M., Leal-Taixé, L., 2019. Understanding the Limitations of CNN-based Absolute Camera Pose Regression, in: Proc. of the IEEE/CVF Intl. Conf. on Computer Vision and Pattern Recognition (CVPR), Long Beach, CA. pp. 3302–3312. doi:10.1109/CVPR.2019.00342.
- Saxena, S., Kar, A., Norouzi, M., Fleet, D.J., 2023. Monocular Depth Estimation using Diffusion Models, in: arXiv preprint arXiv:2302.14816.
- Schönberger, J.L., Frahm, J.M., 2016. Structure-from-Motion Revisited, in: Proc. of the IEEE/CVF Intl. Conf. on Computer Vision and Pattern Recognition (CVPR), Las Vegas, NV. doi:10.1109/CVPR.2016.445.
- Shavit, Y., Ferens, R., Keller, Y., 2022. Learning Multi-Scene Absolute Pose Regression with Transformers, in: Proc. of the IEEE/CVF Intl. Conf. on Computer Vision (ICCV), Montreal, QC. doi:10.1109/ICCV48922.2021.00273.
- Shavit, Y., Keller, Y., 2022. Camera Pose Auto-encoders for Improving Pose Regression, in: Europ. Conf. on Computer Vision (ECCV). doi:10.1007/978-3-031-20080-9_9.
- Shrivastava, A., Pfister, T., Tuzel, O., Susskind, J., Wang, W., Webb, R., 2017. Learning from Simulated and Unsupervised Images Through Adversarial Training, in: Proc. of the IEEE/CVF Intl. Conf. on Computer Vision and Pattern Recognition (CVPR), pp. 2242–2251. doi:10.1109/CVPR.2017.24.
- Stahlke, M., Kram, S., Ott, F., Feigl, T., Mutschler, C., 2022. Estimating TOA Reliability with Variational Autoencoders, in: IEEE Sensors Journal, pp. 5133–5140. doi:10.1109/JSEN.2021.3101933.
- von Stumberg, L., Usenko, V., Cremers, D., 2018. Direct Sparse Visual-Inertial Odometry using Dynamic Marginalization, in: IEEE Intl. Conf. on Robotics and Automation (ICRA), Brisbane, Australia. doi:10.1109/ICRA.2018.8462905.
- von Stumberg, L., Wenzel, P., Yang, N., Cremers, D., 2020. LM-Reloc: Levenberg-Marquardt Based Direct Visual Relocalization, in: IEEE Intl. Conf. on 3D Vision (3DV), Fukuoka, Japan. doi:10.1109/3DV50981.2020.00107.
- Szegedy, C., Liu, W., Jia, Y., Sermanet, P., Reed, S., Anguelov, D., Erhan, D., Vanhoucke, V., Rabinovich, A., 2015. Going Ceepier with Convolutions, in: Proc. of the IEEE/CVF Intl. Conf. on Computer Vision and Pattern Recognition (CVPR), Boston, MA. pp. 1–9. doi:10.1109/CVPR.2015.7298594.
- Tang, W., Long, G., Liu, L., Zhou, T., Blumenstein, M., Jiang, J., 2022. Omni-Scale CNNs: a Simple and Effective Kernel Size Configuration for Time Series Classification, in: Intl. Conf. on Learning Representations (ICLR).
- Tatsunmai, Y., Taki, M., 2022. Sequencer: Deep LSTM for Image Classification, in: Advances in Neural Information Processing Systems (NIPS).
- Valada, A., Radwan, N., Burgard, W., 2018. Deep Auxiliary Learning for Visual Localization and Odometry, in: IEEE Intl. Conf. on Robotics and Automation (ICRA), Brisbane, Australia. pp. 6939–6946. doi:10.1109/ICRA.2018.8462979.
- Venkataraman, H., 2020. 3D Reconstruction Using Structure from Motion, in: Github: <https://github.com/harish-vnkt/structure-from-motion>.
- Wang, J., Qi, Y., 2023. Deep 6-DoF Camera Relocalization in Variable and Dynamic Scenes by Multitask Learning, in: Machine Vision and Applications. doi:10.1007/s00138-023-01388-0.
- Wang, J., Wang, Z., Liu, J., Wu, J., 2018. Multilevel Wavelet Decomposition Network for Interpretable Time Series Analysis, in: ACM Intl. Conf. on Knowledge Discovery & Data Mining (SIGKDD). doi:10.1145/3219819.3220060.
- Wang, S., Clark, R., Wen, H., Trigoni, N., 2017. DeepVO: Towards end-to-end Visual Odometry with deep Recurrent Convolutional Neural Networks, in: IEEE Intl. Conf. on Robotics and Automation (ICRA), Singapore, Singapore. pp. 2043–2050. doi:10.1109/ICRA.2017.7989236.
- Wang, Z., Yan, W., Oates, T., 2016. Time Series Classification from Scratch with Deep Neural Networks: A Strong Baseline, in: arXiv preprint arXiv:1611.06455v4 [cs.LG].
- Winkelbauer, D., Denninger, M., Triebel, R., 2021. Learning to Localize in New Environments from Synthetic Training Data, in: arXiv preprint arXiv:2011.04539v2 [cs.RO]. doi:10.48550/arXiv.2011.04539.
- Xu, M., Wang, Y., Xu, B., Zhang, J., Poslad, J.R.S., Xu, P., 2022. A Critical Analysis of Image-based Camera Pose Estimation Techniques, in: arXiv preprint arXiv:2201.05816v1 [cs.CV].
- Yang, L., Bai, Z., Tang, C., Li, H., Furukawa, Y., Tan, P., 2019. SANet: Scene Agnostic Network for Camera Localization, in: Proc. of the IEEE/CVF Intl. Conf. on Computer Vision (ICCV), Seoul, Korea. doi:10.1109/ICCV.2019.00013.
- Yang, N., von Stumberg, L., Wang, R., Cremers, D., 2020. D3VO: Deep Depth, Deep Pose and Deep Uncertainty for Monocular Visual Odometry, in: Proc. of the IEEE/CVF Intl. Conf. on Computer Vision and Pattern Recognition (CVPR), Seattle, WA. doi:10.1109/CVPR42600.2020.00136.
- Yu, H., Feng, Y., Ye, W., Jiang, M., Bao, H., Zhang, G., 2023. Improving Feature-based Visual Localization by Geometry-Aided Matching, in: arXiv preprint arXiv:2211.08712.v2 [cs.CV]. doi:10.48550/arXiv.2211.08712.
- Yu, Y., Si, X., Hu, C., Zhang, J., 2019. A Review of Recurrent Neural Networks: LSTM Cells and Network Architectures, in: Neural Computation, pp. 1235–1270. doi:10.1162/neco_a_01199.
- Zangeneh, F., Bruns, L., Dekel, A., Pieropan, A., Jensfelt, P., 2023. A Probabilistic Framework for Visual Localization in Ambiguous Scenes, in: arXiv preprint arXiv:2301.02086 [cs.CV]. doi:10.48550/arXiv.2301.02086.
- Zerveas, G., Jayaraman, S., Patel, D., Bhamidipaty, A., Eickhoff, C., 2021. A Transformer-based Framework for Multivariate Time Series Representation Learning, in: Proc. of the ACM Intl. Conf. on Knowledge Discovery & Data Mining (SIGKDD), pp. 2114–2124. doi:10.1145/3447548.3467401.
- Zhan, H., Weerasekera, C.S., Bian, J.W., Reid, I., 2020. Visual Odometry Revisited: What Should Be Learnt?, in: IEEE Intl. Conf. on Robotics and Automation (ICRA), Paris, France. doi:10.1109/ICRA40945.2020.9197374.
- Zhang, C., Bengio, S., Hardt, M., Recht, B., Vinyals, O., 2017. Understanding Deep Learning (still) Requires Rethinking Generalization, in: Communications of the ACM, pp. 107–115. doi:10.1145/3446776.
- Zhang, N., Nex, F., Vosselman, G., Kerle, N., 2023. Lite-Mono: A Lightweight CNN and Transformer Architecture for Self-Supervised Monocular Depth Estimation, in: Proc. of the IEEE/CVF Intl. Conf. on Computer Vision and Pattern Recognition (CVPR), pp. 18537–18546.
- Zheng, L., Yang, Y., Tian, Q., 2018. SIFT Meets CNN: A Decade Survey of Instance Retrieval, in: IEEE Trans. on Pattern Analysis and Machine Intelligence (TPAMI), pp. 1224–1244.
- Zhi-Yu, C., Po-Heng, C., Kuan-Wen, C., Chen-Yu, C., 2021. PA-FlowNet: Pose-Auxiliary Optical Flow Network for Spacecraft Relative Pose Estimation, in: Proc. of the IAPR Intl. Conf. on Pattern Recognition (ICPR). doi:10.1109/ICPR48806.2021.9413201.
- Zhou, G.B., Wu, J., Zhang, C.L., Zhou, Z.H., 2016. Minimal Gated Unit for Recurrent Neural Networks, in: Intl. Journal of Automation and Computing (IJAC), pp. 226–234. doi:doi.org/10.1007/s11633-016-1006-2.
- Zhou, L., Luo, Z., Shen, T., Zhang, J., Zhen, M., Yao, Y., Fang, T., Quan, L., 2020. KFNet: Learning Temporal Camera Relocalization using Kalman Filtering, in: Proc. of the IEEE/CVF Intl. Conf. on Computer Vision and Pattern Recognition (CVPR), Seattle, WA. pp. 4919–4928. doi:10.1109/CVPR42600.2020.00497.
- Zou, X., Wang, Z., Li, Q., Sheng, W., 2019. Integration of Residual Network and Convolutional Neural Network Along with Various Activation Functions and Global Pooling for Time Series Classification, in: Neurocomputing, pp. 39–45. doi:10.1016/j.neucom.2019.08.023.

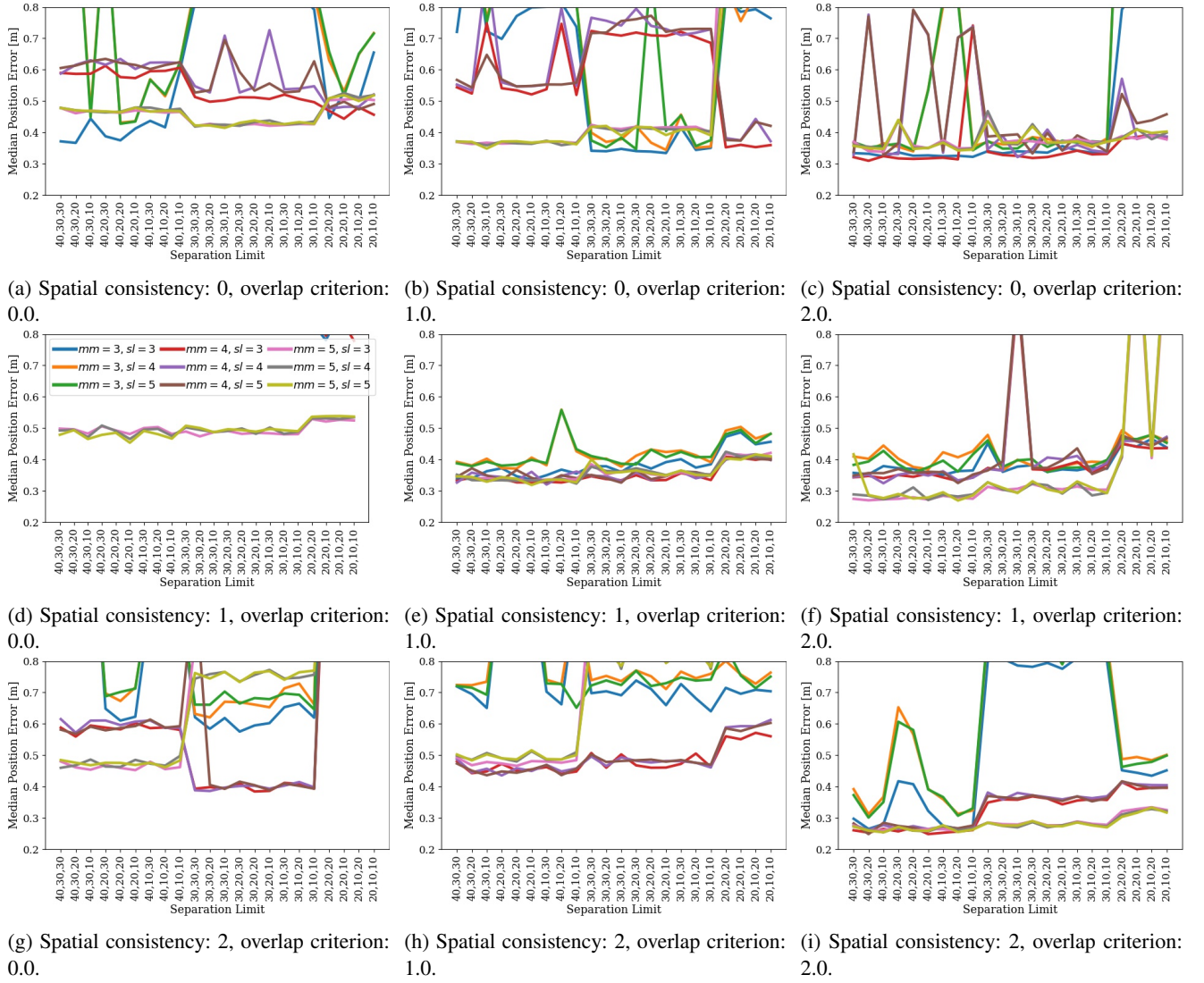


Figure 27: Detailed evaluation results for the SfM hyperparameter search for the robot train 3 and test 6 datasets. Median position error in m . For readability, the label spacing is fixed. The legend shows the *minimum matches* hyperparameter. The legend is equal for all subplots.

A. Appendix A

A.1. Hyperparameter Search

In Figure 27 and Figure 28, we conduct a detailed hyperparameter search for the robot dataset, while in Figure 29 and Figure 30, we perform a similar search for the handheld dataset. The x-axis of each figure represents a combination of three hyperparameters (ex_1, ex_2, ex_3) that control the separation limit. We search for each of these parameters in the range of $[10, 20, 30, 40]$, subject to the constraints that $ex_1 \geq ex_2$, $ex_1 \geq ex_3$, and $ex_2 \geq ex_3$. Here, ex_1 is the cluster separation limit, ex_2 is the Gibbs separation parameter, and ex_3 is the 3D position adjustment of BA. We observe that certain combinations of these parameters result in high error rates, but higher values of the parameters generally yield lower position and orientation errors. For example, $(ex_1, ex_2, ex_3) = (40, 30, 30)$ produces the best results.

For each combination of hyperparameters, we generate a point cloud using the parameters $mm \in [3, 4, 5]$, $sl = std \in [3, 4, 5]$, the spatial consistency $sc \in [0, 1, 2]$, and the overlap criterion $oc \in [0.0, 0.1, 0.2]$. For the robot dataset, we found that the combination of $sc = 2$ and $oc = 2.0$ yields the best results (position error below $0.3m$ and orientation error below 1.5°), as depicted in Figure 27i and Figure 28i. For the handheld dataset, we recommend the combination of $sc = 1$ and $oc = 1.0$, refer to Figure 29e and Figure 30e. We also observe that a high value for the minimum matches parameter $mm = 5$ is clearly the best choice, while $std = [3, 4, 5]$ produces similar results.

A.2. Trajectory Plots

Figure 31 to Figure 38 contain visualizations of the predicted absolute poses for SfM, encompassing all eight training datasets and ten test datasets.

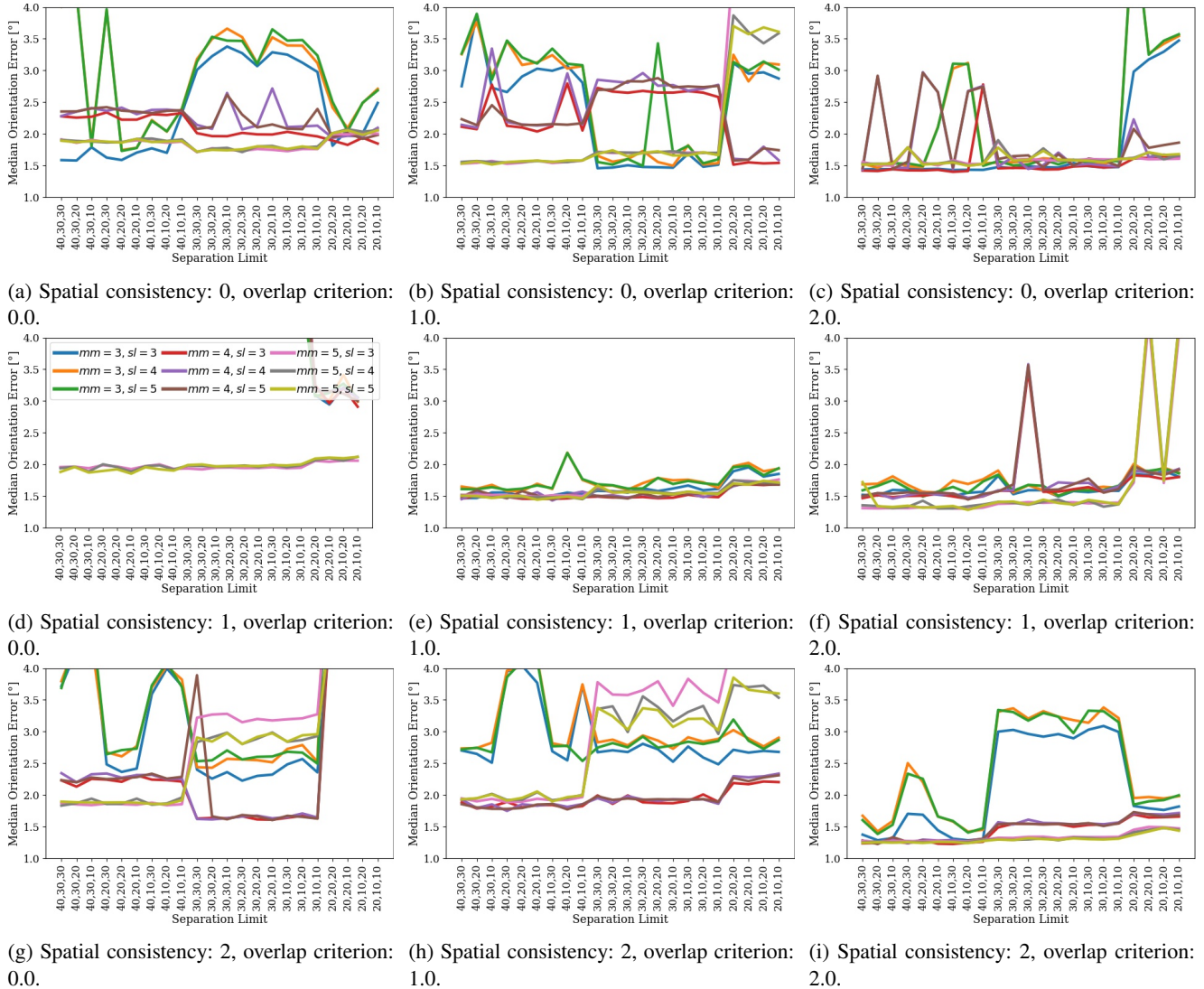


Figure 28: Detailed evaluation results for the SfM hyperparameter search for the robot train 3 and test 6 datasets. Median orientation error in $^{\circ}$. For readability, the label spacing is fixed. The legend shows the *minimum matches* hyperparameter. The legend is equal for all subplots.

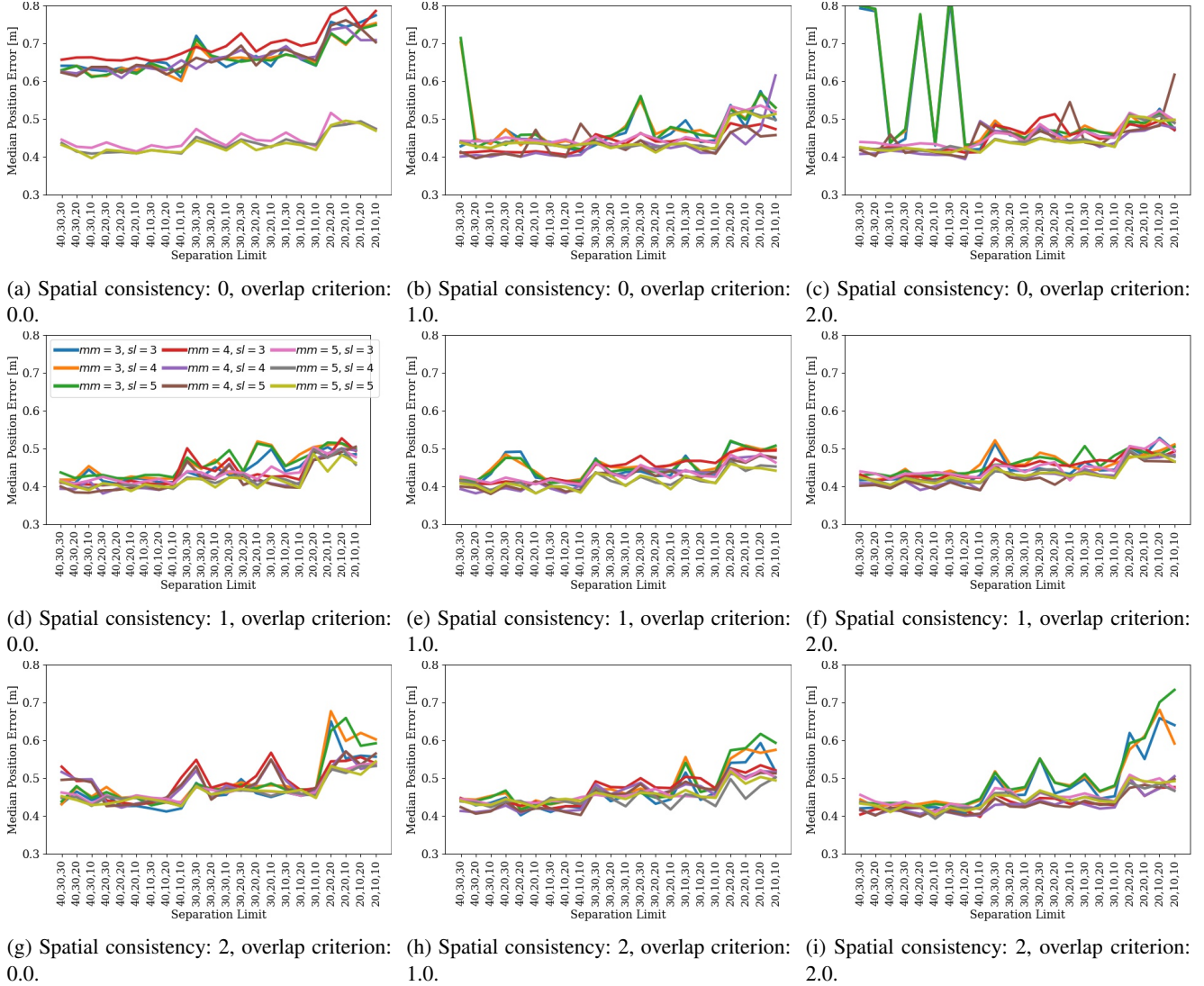


Figure 29: Detailed evaluation results for the SfM hyperparameter search for the handheld train 4 and test 7 datasets. Median position error in m . For readability, the label spacing is fixed. The legend shows the *minimum matches* hyperparameter. The legend is equal for all subplots.

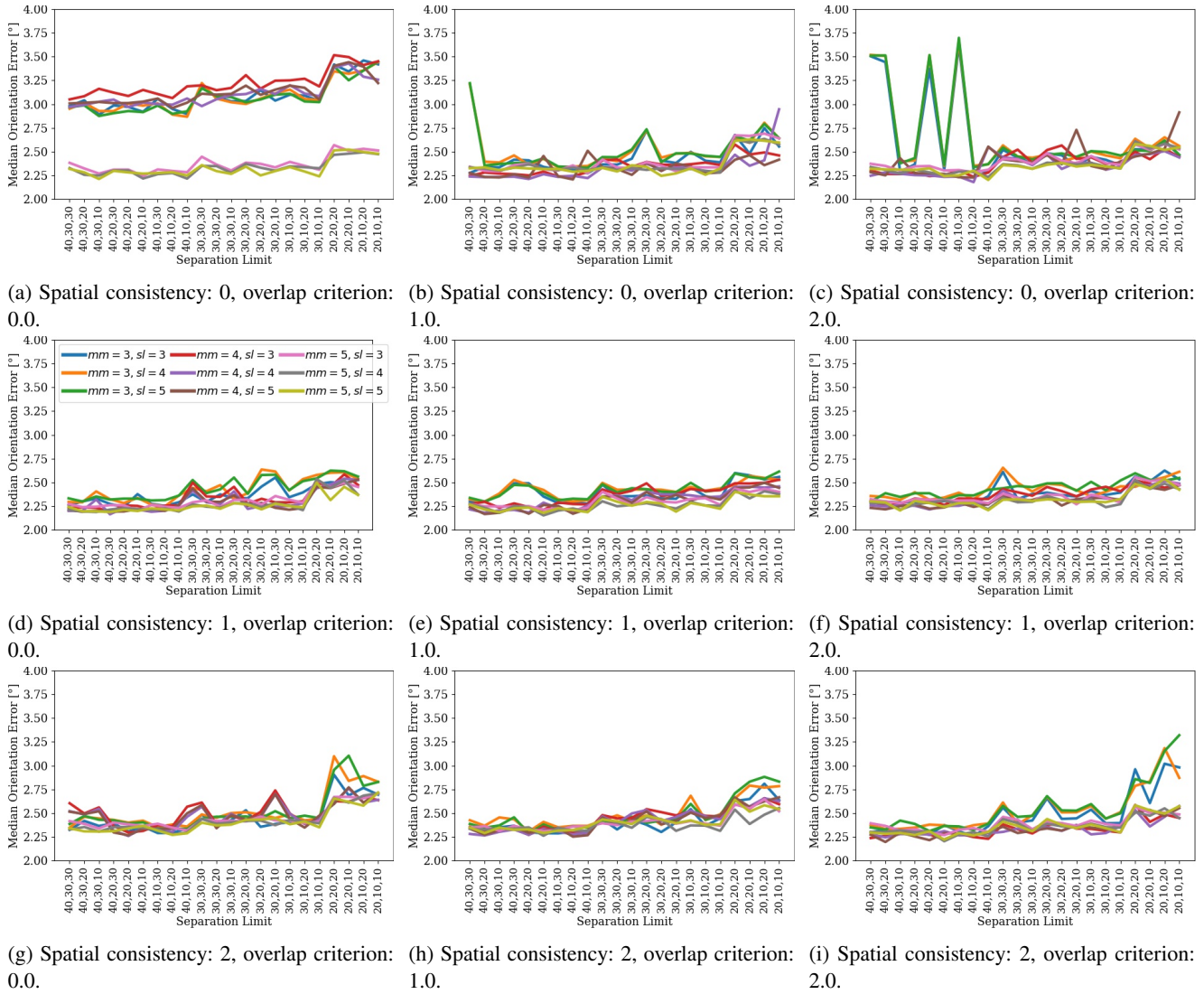


Figure 30: Detailed evaluation results for the SfM hyperparameter search for the handheld train 4 and test 7 datasets. Median orientation error in $^{\circ}$. For readability, the label spacing is fixed. The legend shows the *minimum matches* hyperparameter. The legend is equal for all subplots.

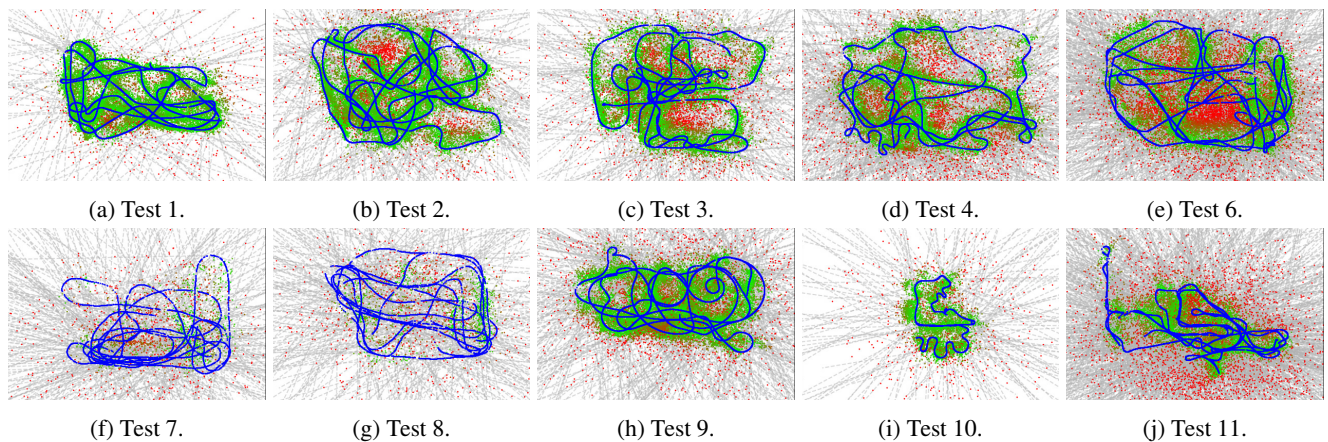


Figure 31: Evaluation of the predicted positions (green, red) against the ground truth trajectories (blue) for SfM for the train 1 dataset.

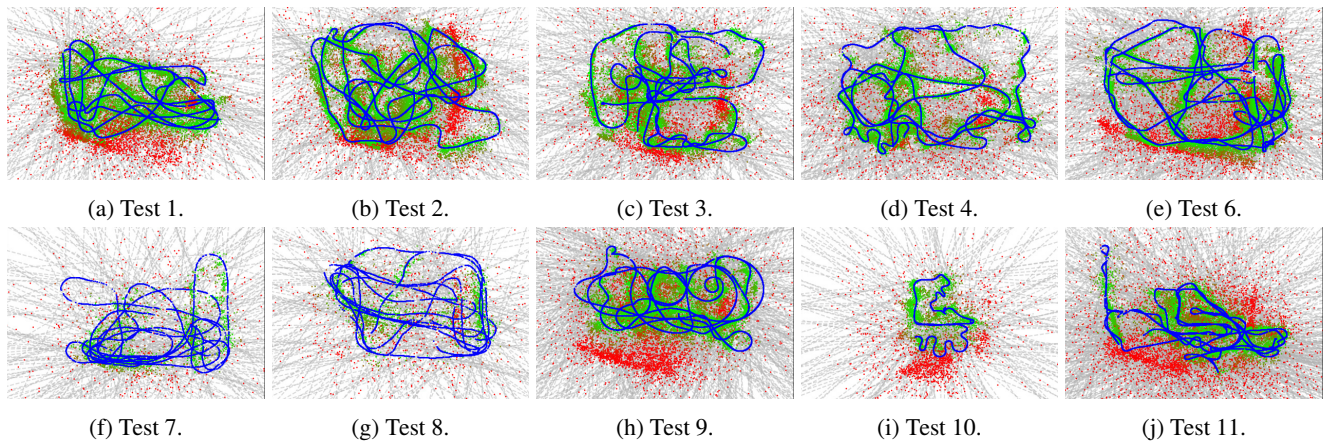


Figure 32: Evaluation of the predicted positions (green, red) against the ground truth trajectories (blue) for SfM for the train 2 dataset.

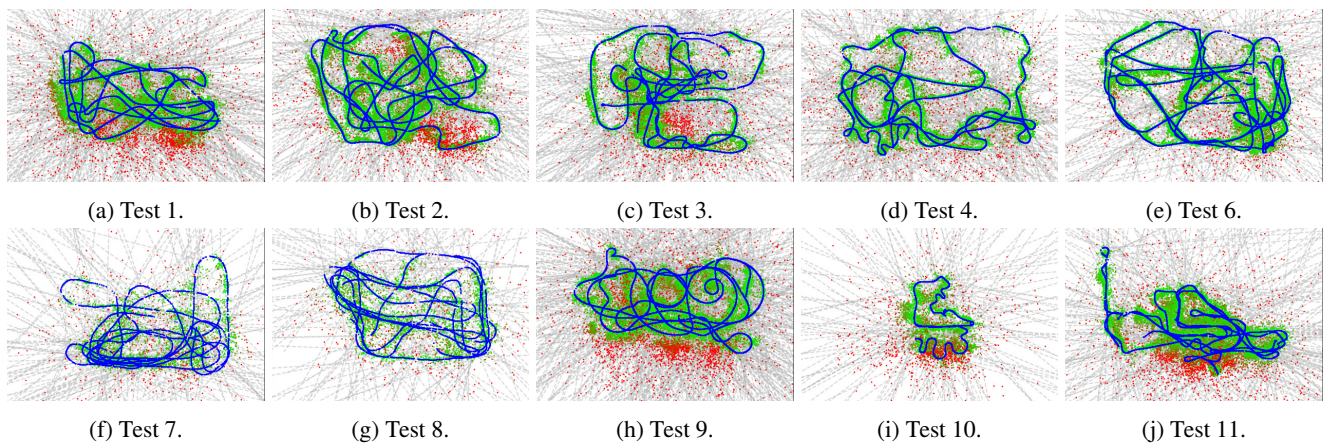


Figure 33: Evaluation of the predicted positions (green, red) against the ground truth trajectories (blue) for SfM for the train 3 dataset.

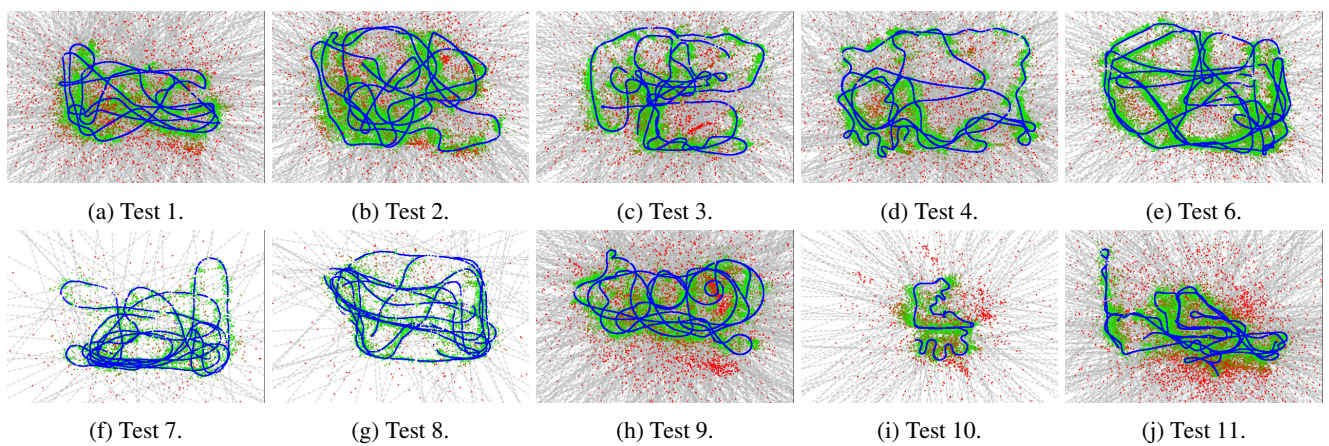


Figure 34: Evaluation of the predicted positions (green, red) against the ground truth trajectories (blue) for SfM for the train 4 dataset.

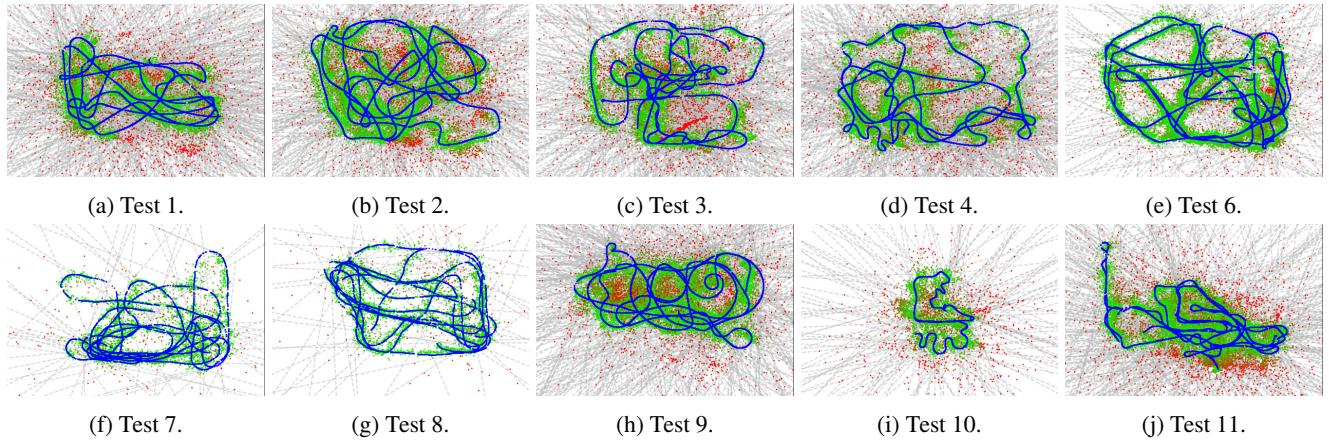


Figure 35: Evaluation of the predicted positions (green, red) against the ground truth trajectories (blue) for SfM for the train 5 dataset.

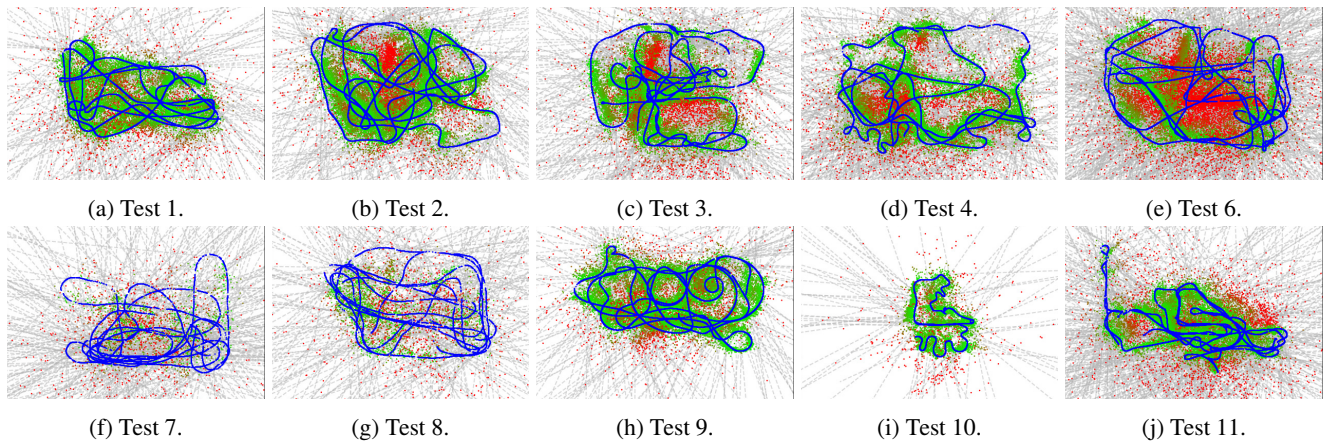


Figure 36: Evaluation of the predicted positions (green, red) against the ground truth trajectories (blue) for SfM for the train 6 dataset.

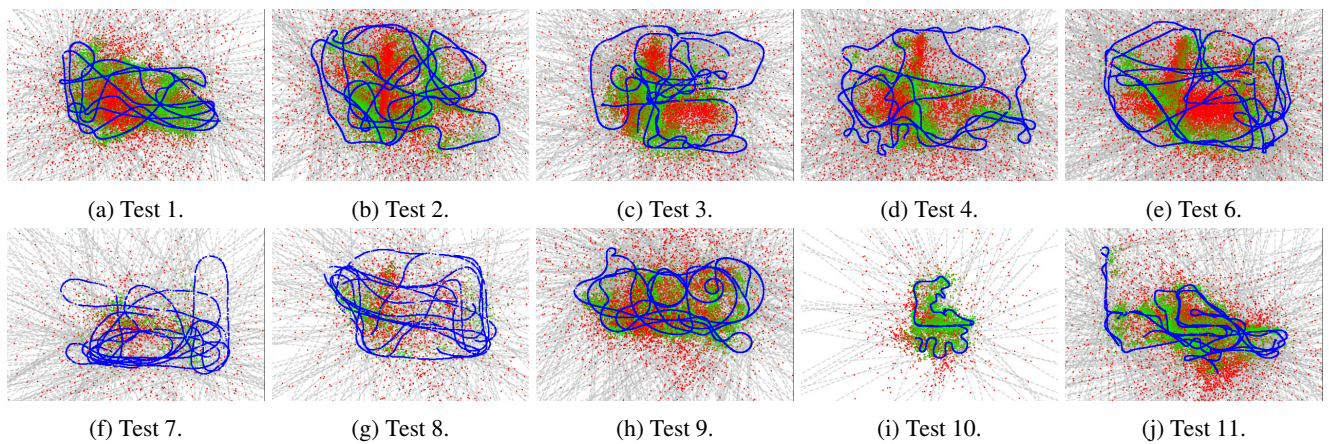


Figure 37: Evaluation of the predicted positions (green, red) against the ground truth trajectories (blue) for SfM for the train 7 dataset.

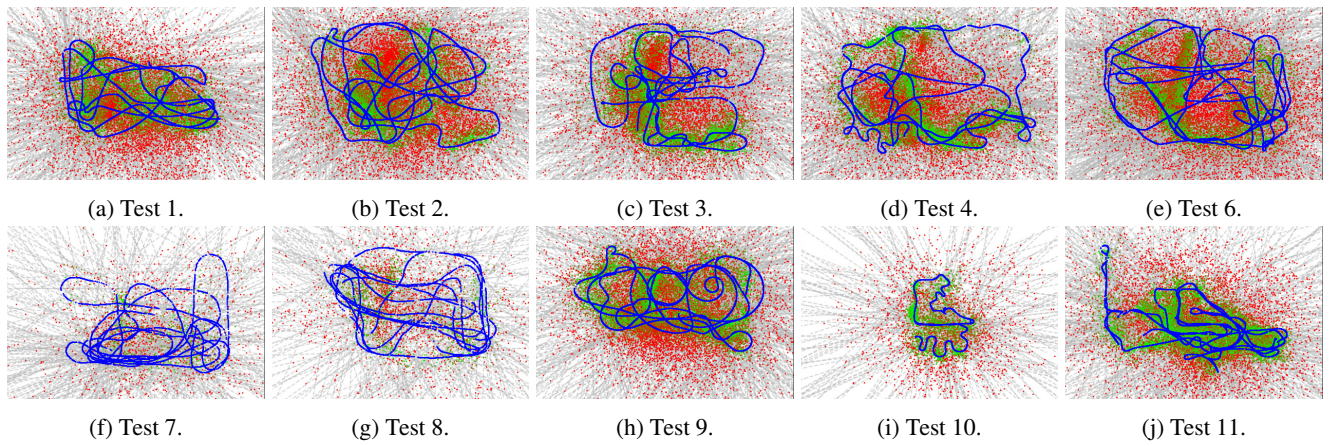


Figure 38: Evaluation of the predicted positions (green, red) against the ground truth trajectories (blue) for SfM for the train 8 dataset.

Biography



Felix Ott received his MSc. degree in Computational Engineering at the FAU Erlangen-Nürnberg in 2019. He joined the Hybrid Positioning & Information Fusion group in the Locating and Communication Systems department at Fraunhofer IIS. In 2023 he received his Ph.D. at the Ludwig-Maximilians University in Munich working in the Probabilistic Machine and Deep Learning group. His research covers multimodal information fusion for self-localization.



Lucas Heublein received his M.Sc. degree in Integrated Life Science at the FAU Erlangen-Nürnberg. In 2020, he started his Computer Science degree at the FAU. He joined the Hybrid Positioning & Information Fusion group at the Fraunhofer IIS in 2020 as a student assistant.



David Rügamer is an interim professor for Computational Statistics at the RWTH Aachen. Before he was research associate, lecturer and interim professor for Data Science at the LMU Munich, where he also received his Ph.D. in 2018. His research is concerned with scalability of statistical modeling as well as machine learning for functional and multimodal data.



Bernd Bischl is a full professor for statistical learning and data science and a director of the Munich Center of Machine Learning. His research focuses amongst other things on AutoML, interpretable machine learning and ML benchmarking.



Christopher Mutschler leads the precise positioning and analytics department at Fraunhofer IIS. Prior to that, Christopher headed the Machine Learning & Information Fusion group. He gives lectures on machine learning at the FAU Erlangen-Nürnberg (FAU), from which he also received both his Diploma and PhD in 2010 and 2014 respectively. Christopher's research combines machine learning with radio-based localization.